Microphysics-based Black Carbon Aging in a global CTM: Constraints from HIPPO Observations and Implications for Global Black Carbon Budget

Cenlin He[1], Qinbin Li[1], Kuo-Nan Liou[1], Ling Qi[1], Shu Tao[2], Joshua P. Schwarz[3]

[1]Department of Atmospheric and Oceanic Sciences and Joint Institute for Regional Earth System Science and Engineering, University of California, Los Angeles (UCLA), Los Angeles, CA 90095, USA

[2]Laboratory for Earth Surface Processes, College of Urban and Environmental Sciences, Peking University, Beijing 100871, China

[3]Chemical Sciences Division, Earth System Research Laboratory, NOAA, Boulder, CO 80305, USA

Correspondence to: Cenlin He (cenlinhe@atmos.ucla.edu)

Abstract

We develop and examine a microphysics-based black carbon (BC) aerosol aging scheme that accounts for condensation, coagulation, and heterogeneous chemical oxidation processes in a global 3-D chemical transport model (GEOS-Chem) by interpreting the BC measurements from the HIAPER Pole-to-Pole Observations (HIPPO, 2009–2011) using the model. We convert aerosol mass in the model to number concentration by assuming lognormal aerosol size distributions and compute the microphysical BC aging rate (excluding chemical oxidation aging) explicitly from the condensation of soluble materials onto hydrophobic BC and the coagulation between hydrophobic BC and preexisting soluble particles. The chemical oxidation aging is tested in the sensitivity simulation. The microphysical aging rate is ~4 times higher in the lower troposphere over source regions than that from a fixed aging scheme with an e-folding time of 1.2 days. The higher aging rate reflects the large emissions of sulfate-nitrate and secondary organic aerosol precursors hence faster BC aging through condensation and coagulation. In contrast, the microphysical aging is more than fivefold slower than the fixed aging in remote regions, where condensation and coagulation are weak. Globally BC microphysical aging is dominated by condensation, while coagulation contribution is largest over East China, India, and Central Africa. The fixed aging scheme results in an overestimate of HIPPO BC throughout the troposphere by a factor of 6 on average. The microphysical scheme reduces this discrepancy by a factor of ~3, particularly in the middle and upper troposphere. It also leads to a threefold reduction in model bias in the latitudinal BC column burden averaged along the HIPPO flight tracks, with largest improvements in the tropics. The resulting global annual mean BC lifetime is 4.2 days and BC burden is 0.25 mg m^{-2}, with 7.3% of the burden at high altitudes (above 5 km). Wet scavenging accounts for 80.3% of global BC deposition. We find that in source regions the microphysical aging rate is insensitive to aerosol size distribution, condensation threshold, and chemical oxidation aging, while it is the opposite in remote

45 regions, where the aging rate is orders of magnitude smaller. As a result, global BC
46 burden and lifetime show little sensitivity (<5% change) to these three factors.
47

1. Introduction

Black carbon (BC) aerosol is one of the most important contributors to current global and regional warming (Bond et al., 2013). BC directly absorbs solar radiation, leading to significant atmospheric warming (Ramanathan and Carmichael, 2008). It also acts as cloud condensation nuclei (CCN), affecting cloud formation and distribution (Jacobson, 2014). Additionally, BC reduces snow albedo after deposition on snow, resulting in accelerated snow melting (Painter et al., 2013; Liou et al., 2014). The assessment by Bond et al. (2013) pointed out that current estimates of BC climatic effects involve large uncertainties. One of the critical uncertainty sources is BC atmospheric aging through the physical and chemical transformation of BC from hydrophobic to hydrophilic particles.

BC is emitted mostly as hydrophobic particles externally mixed with other aerosol constituents (Zhang et al., 2008). Recent studies showed that BC can also be frequently mixed with organics even at emission under specific conditions (Willis et al., 2015 and references therein). Hydrophobic BC becomes hydrophilic due to increasing internal mixing with water-soluble materials through condensation (Moteki et al., 2007), coagulation (Johnson et al., 2005), and heterogeneous oxidation (Khalizov et al., 2010) during atmospheric aging. Hereinafter we refer to these internal mixtures generically as "coatings" without making any specific reference to mixing morphology. Coating enhances BC absorption and scattering capacities (Bond et al., 2006), which depends on coating properties and particle morphology (Scarnato et al., 2013; He et al., 2015). Coated BC particles typically have a higher hygroscopicity (Zhang et al., 2008) and hence more efficient wet scavenging, which further affects BC atmospheric lifetime (Zhang et al., 2015). Thus, BC aging is expected to play a critical role in affecting both BC optical properties and global distribution.

In global chemical transport models (CTMs), BC aging is typically parameterized by a

fixed e-folding time of 1–2 days for the hydrophobic-to-hydrophilic BC conversion (e.g., Chung and Seinfeld, 2002; Koch et al., 2009; Q. Q. Wang et al., 2011, 2014). However, Koch et al. (2009) and Schwarz et al. (2013) showed that most global models significantly deviate from observed global BC distributions. It is likely that the prescription of uniform BC aging timescales may be partially contributing to such biases. In this vein, Shen et al. (2014) optimized the fixed e-folding aging time of BC by fitting a global CTM results to HIPPO observations. They suggested that anthropogenic BC from East Asia ages much faster than one day, while the aging of biomass burning BC from Southeast Asia is much slower. Using another global CTM constrained by HIPPO observations, Zhang et al. (2015) pointed out that the optimized e-folding aging time following Shen et al. (2014) varies significantly for BC emitted from different source regions, with less than half a day for BC emitted from the tropics and mid-latitudes and ~1 week for BC emitted from high latitudes. Thus, a uniform BC aging time is likely not representative and can conceivably lead to large uncertainties.

In addition, field measurements have shown that a fixed e-folding time of 1–2 days underestimates the BC aging rate in polluted areas and is unrepresentative under complex atmospheric conditions. For example, Johnson et al. (2005) found that ambient BC particles that underwent aging for less than a few hours were heavily coated in Mexico City, primarily with ammonium sulfate. Schwarz et al. (2008) showed that 60–80% of BC particles are coated in fresh emissions from biomass burning sources. Moffet and Prather (2009) observed a BC aging time of ~3 hours in Mexico City under photochemically active conditions. Akagi et al. (2012) showed that the fraction of coated BC particles produced from a chaparral fire in California increased up to ~85% over a 4-hour period. Therefore, it is imperative to better capture BC aging rate under different atmospheric conditions in order to accurately estimate BC spatiotemporal distribution and consequently its radiative effects.

To that end, several global models have treated BC aging with size-resolved aerosol microphysics (e.g., Jacobson, 2010; Aquila et al., 2011). Many global models still rely on relatively simple parameterizations for BC aging (e.g., Riemer et al., 2004; Liu et al., 2011; Oshima and Koike, 2013) in part for computational efficiency consideration. For example, Riemer et al. (2004) developed a BC aging parameterization in which aging rate was a function of total number concentration of secondary inorganic particles and internally mixed BC particles, representing the effects of condensation and coagulation processes. Liu et al. (2011) proposed another parameterization in which BC aging rate was a linear function of hydroxyl radical (OH) concentration (i.e., a fast-aging term representing condensation of sulfuric acid) with a constant slow-aging term (e.g., coagulation). Croft et al. (2005) and Huang et al. (2013) further employed these two parameterizations in a global model to estimate aging effects on BC budget and lifetime. However, there are limitations in these simplified aging parameterizations. The Riemer et al. (2004) parameterization was designed specifically for domains dominated by fossil fuel emissions, which may not be suitable for application to a global scale. The Liu et al. (2011) formulation neglected the dependencies of BC aging on different condensable materials and their precursors (e.g., SO_2). Furthermore, under complex atmospheric conditions, these parameterizations likely introduce large uncertainties by lumping microphysical details of BC aging into a few parameters. Incorporating explicit microphysical representations of the BC aging process in global models may partially rectify and reduce the uncertainties.

In this study, we develop a "hybrid" microphysics-based BC aging scheme that accounts for condensation and coagulation processes in the GEOS-Chem global 3-D CTM. GEOS-Chem has been widely used to simulate BC in source regions (Li et al., 2015), continental outflows (Park et al., 2005), remote mountainous regions (He et al., 2014a),

the Arctic (Wang et al., 2011), and remote oceans (Q. Q. Wang et al., 2014). Presently GEOS-Chem employs a fixed e-folding time of 1.2 days for the BC aging (Park et al., 2003). We convert aerosol mass in the model to number concentration by assuming lognormal aerosol size distributions and explicitly compute the microphysical BC aging rate from the condensation of soluble materials onto hydrophobic BC and the coagulation between hydrophobic BC and preexisting hydrophilic particles. The 'hybrid' microphysical aging scheme thus not only takes account of the microphysical aging processes but also avoids the use of full-fledged dynamic aerosol microphysics thereby retains the computational efficiency of the fixed e-folding time aging scheme. The 'hybrid' microphysical aging scheme can be similarly applied in other CTMs. We systematically examine BC simulations using the aging scheme by comparison with the HIAPER Pole-to-Pole Observations (HIPPO) of BC during 2009–2011. We further analyze the effects of the aging scheme on global BC lifetime and budget. Finally, we quantify the uncertainties associated with key parameters in the aging scheme and the effects of chemical oxidation on BC aging.

2. Methods

2.1 Observations

We use the HIPPO aircraft measurements (Wofsy et al., 2011) of BC in this study. HIPPO (http://hippo.ornl.gov/) provides unique constraints on BC distributions from the surface up to ~14 km across the Pacific from 67°S to 85°N latitudes. There were five deployments during 2009–2011 (Fig.1, HIPPO 1: January 8–30, 2009; HIPPO 2: October 30 – November 22, 2009; HIPPO 3: March 24 – April 16, 2010; HIPPO 4: June 14 – July 11, 2011; HIPPO 5: August 9 – September 9, 2011). The refractory BC (rBC) mass concentration was measured by a single-particle soot photometer (SP2) that detects individual particles (Schwarz et al., 2010, 2013). SP2 measures rBC in a mass range corresponding to volume-equivalent diameter range of ~90–550 nm assuming 1.8 g/cc

void free density. This range contains about 90% of the total BC mass in the accumulation mode. The observed rBC concentration was scaled upwards by 10% to account for BC particles undetected by SP2 (Schwarz et al., 2010) in this mode. rBC is experimentally equivalent to elemental carbon at the 15 % level (Kondo et al., 2011), and hence is equivalent to BC in the model. The effective detection limit (2σ level) is 0.01 ng kg^{-1} (0.1 ng kg^{-1}) for 15-minute (1-minute) sampling at low altitudes and increase to 0.05 (0.5 ng kg^{-1}) at the higher altitudes (Schwarz et al., 2013). The SP2 measurement of rBC mass is insensitive to non-BC mass and not influenced by other absorbing particles such as dust or non-absorbing species including salt and sulfate. Schwarz et al. (2013) determined a total systematic uncertainty of 30% associated with rBC mass concentration measured with the SP2. Schwarz et al. (2010, 2013) provided details of the BC measurement during HIPPO. We average the BC observations that are located within each model grid and over the model transport time step (15 minutes), thus ensuring a consistent spatiotemporal resolution for direct comparison with the model results.

2.2 Model description and simulations

In this study, we use the GEOS-Chem model (version 9-01-03) driven by assimilated meteorological fields from the Goddard Earth Observing System (GEOS-5) of the NASA Global Modeling and Assimilating Office (GMAO). GEOS-5 meteorological fields have a 6-hour temporal resolution (3 hours for surface variables and mixing depths), a native horizontal resolution of 0.5°×0.667°, and 72 vertical layers (from the surface to 0.01 hPa). The spatial resolution is degraded to 2°×2.5° horizontally and 47 layers vertically for computational efficiency. GEOS-Chem includes a fully coupled treatment of tropospheric O_3-NO_x-VOC chemistry, sulfate-nitrate-ammonia and carbonaceous aerosols. Park et al. (2003) presented the first GEOS-Chem simulation of carbonaceous aerosols including BC and organic carbon (OC). The model also accounts for other aerosols including secondary organic aerosol (SOA), dust, and sea salt. GEOS-Chem uses a bulk aerosol

scheme that separately tracks mass concentrations of different aerosol species (i.e., externally mixed). The model resolves hydrophobic and hydrophilic BC and OC, fine-mode (0.01–0.5 μm) and coarse-mode (0.5–8.0 μm) sea salt, dust in four size bins (0.1–1.0, 1.0–1.8, 1.8–3.0, and 3.0–6.0 μm), and five types of lumped SOA formed from different precursors. Aerosol and gas phase simulations are coupled through formation of sulfate, nitrate, and SOA, heterogeneous chemistry, and aerosol effects on photolysis rates. Details on the GEOS-Chem aerosol simulations are provided, respectively, by Park et al. (2003) for BC and OC, Park et al. (2004) for sulfate-nitrate-ammonia, Liao et al. (2007) for SOA, Fairlie et al. (2007) for dust, and Alexander et al. (2005) for sea salt.

2.2.1 A microphysics-based BC aging scheme

We assume that 80% of freshly emitted BC particles are hydrophobic (Cooke et al., 1999; Park et al., 2003). Presently BC aging process is not explicitly represented in GEOS-Chem. Instead, a fixed e-folding time (τ) of 1.2 days is assumed for the hydrophobic-to-hydrophilic BC conversion in the forms (Park et al., 2003):

$$\left(\frac{dm_{BCPO}}{dt}\right) = -\frac{m_{BCPO}}{\tau} \quad (1)$$

$$\left(\frac{dm_{BCPI}}{dt}\right) = -\left(\frac{dm_{BCPO}}{dt}\right) \quad (2)$$

where m_{BCPO} and m_{BCPI} are the mass concentration of hydrophobic (BCPO) and hydrophilic BC (BCPI), respectively. In this study, we develop a microphysics-based BC aging scheme in the model by explicitly accounting for both condensation and coagulation processes. This microphysical aging scheme can be similarly applied in other CTMs. Additionally, we incorporate an experiment-based parameterization for BC aging through heterogeneous chemical oxidation (Pöschl et al., 2001) for comparison and contrast.

2.2.1.1 Condensation

The condensation rate of a gaseous species (*A*) onto an individual particle can be expressed as follows (Seinfeld and Pandis, 2006):

$$J_{A,p} = 4\pi f(K_n,\alpha) R_p D_{f_A} (c_\infty - c_s) \quad (3)$$

$$f(K_n,\alpha) = \frac{1+K_n}{1+2K_n(1+K_n)/\alpha} \quad (4)$$

where $J_{A,p}$ is the condensation rate (mol s^{-1}) of *A* onto a particle, R_p represents the particle radius (m), D_{f_A} is the gas-phase diffusivity (m^2 s^{-1}) of *A*, c_∞ and c_s are gas-phase concentrations (mol m^{-3}) of *A* far from the particle and at the particle surface, respectively. K_n is the Knudsen number (i.e., ratio of air mean free path to particle radius), α is the accommodation coefficient (α = 1 in this study), and $f(K_n, \alpha)$ is the correction factor for non-continuum effects and imperfect surface accommodation based on the mathematical expression from Dahneke (1983). The mass of *A* condensing onto BCPO in a model grid per unit time, k_A, can be calculated by the product of the total available mass of *A* for condensing onto all pre-existing aerosols and the fraction of condensed mass partitioned to BCPO, which depends on condensation rate (*J*) and particle number concentration (*N*) as follows:

$$k_A = \frac{J_{A,BCPO,tot}}{\sum_{p_{i=1}}^{p_{i=7}} J_{A,p_i,tot}} M_{A,cond} = \frac{\int_0^\infty n_{BCPO}(R_{BCPO}) f_{BCPO}(K_n,\alpha) R_{BCPO} dR_{BCPO}}{\sum_{p_{i=1}}^{p_{i=7}} \int_0^\infty n_{p_i}(R_{p_i}) f_{p_i}(K_n,\alpha) R_{p_i} dR_{p_i}} M_{A,cond} \quad (5)$$

where p_i (i = 1–7) represents seven types of pre-existing aerosols (i.e., BCPO, BCPI, hydrophobic OC, hydrophilic OC, sulfate, fine-mode and coarse-mode sea salt) available for condensation, $J_{A,p_i,tot}$ is the condensation rate of *A* onto particle p_i, $M_{A,cond}$ is the total condensed mass of *A* in a model grid per unit time, R_{p_i} and n_{p_i} (= dN_{p_i}/dR_{p_i}) are the radius and number concentration distribution function of pre-existing particles, respectively. We account for condensation of gaseous sulfuric acid (H_2SO_4), nitric acid (HNO_3), ammonia (NH_3), and SOA onto pre-existing BC, OC, sulfate (SO_4^{2-}, NO_3^-, and

232 NH_4^+), and sea salt aerosols.

233

234 GEOS-Chem tracks only aerosol mass concentration rather than number concentration
235 that is required in Eq. (4). We convert aerosol mass concentration (m_{p_i}) to number
236 concentration (N_{p_i}), assuming lognormal distributions for different aerosols following
237 Croft et al. (2005) in the form:

238 $$N_{p_i} = \frac{m_{p_i}}{\rho_{p_i}} \left(\frac{\pi}{6} D_{p_i}^3 \exp\left(\frac{9}{2} \ln^2 \sigma_{p_i}\right)\right)^{-1} \quad (6)$$

239 where ρ_{p_i} is the particle density (1.8 g cm^{-3} for BC and OC, 1.7 g cm^{-3} for sulfate, and
240 2.2 g cm^{-3} for sea salt), D_{p_i} and σ_{p_i} are the geometric mean diameter and standard
241 deviation of number size distribution, respectively. Following Dentener et al. (2006) and
242 Yu and Luo (2009), we assume D_p = 60 nm and σ_p = 1.8 for BCPO and hydrophobic OC,
243 and D_p = 150 nm and σ_p = 1.8 for BCPI and hydrophilic OC (Table 1). We use size
244 distributions from the Global Aerosol Dataset (GADS) (Koepke et al., 1997) for sulfate
245 (D_p = 150 nm, σ_p = 1.6), fine sea salt (D_p = 200 nm, σ_p = 1.5), and coarse sea salt (D_p =
246 800 nm, σ_p = 1.8). In order to analytically compute the integral in Eq. (5), we have
247 assumed a constant correction factor $f(K_n, \alpha)$ for each type of aerosols with different sizes,
248 which may introduce uncertainty in the computation. Under this assumption and using a
249 lognormal aerosol size distribution, the integral can now be computed by following the
250 mathematical identity:

251 $$\int_0^\infty n_{p_i}(R_{p_i}) R_{p_i} dR_{p_i} = N_{p_i} \frac{D_{p_i}}{2} \exp\left(\frac{1}{2} \ln^2 \sigma_{p_i}\right) \quad (7)$$

252 The hydrophobic-to-hydrophilic BC conversion rate (kg m^{-3} s^{-1}) due to condensation can
253 be written as

254 $$\left(\frac{dm_{BCPO}}{dt}\right)_{cond} = -\frac{F_{BCPO->BCPI} m_{BCPO}}{\Delta t} \quad (8)$$

$$F_{BCPO->BCPI} = \frac{\sum_{A_i=1}^{A_i=4} k_{A_i} \cdot \Delta t}{\beta M_{BCPO}} \quad (9)$$

where $F_{BCPO->BCPI}$ represents the fraction of BCPO becoming BCPI through condensation of four types of soluble species A_i (i = 1–4, i.e., H_2SO_4, HNO_3, NH_3, and SOA) in a model time step (Δt). This implicitly assumes that different secondary aerosol species have the same hygroscopicity. We note that some SOA species could be less hygroscopic than ammonia sulfate (Prenni et al., 2007). m_{BCPO} is BCPO mass concentration (kg m^{-3}), M_{BCPO} is the total BCPO mass (kg) in a model grid, and β is the condensation threshold (i.e., the mass fraction of condensed soluble materials on BCPO required for the hydrophobic-to-hydrophilic conversion). Following Riemer et al. (2004), we set β = 5% in the standard simulation based on hygroscopic growth behavior of aerosols (Weingartner et al., 1997). After the hydrophobic-to-hydrophilic BC conversion, we lump the mass of secondary aerosol material coated on BC with those not mixed with BC in order to be compatible with the bulk aerosol scheme in GEOS-Chem, where the mass concentration of different aerosol species are separately tracked. The lumping, instead of treating coating materials and hydrophilic BC together, only introduces small uncertainty, considering that the size distribution of hydrophilic BC is similar to that of SOA and sulfate in this study (see Table 1). Further sensitivity analysis also show minor effects of the hydrophilic aerosol size distribution on global BC concentration and lifetime (see Sect. 4.3). The use of global uniform particle size distributions and β value can conceivably introduce large uncertainties. To quantify the uncertainties, we conduct additional model simulations by varying the size distribution and β value (see Table 1 and Sect. 4).

2.2.1.2 Coagulation

The coagulation rate ($J_{BCPO,X,}$ m^{-3} s^{-1}) between BCPO and hydrophilic particles (X) can be expressed by (Seinfeld and Pandis, 2006)

$$J_{BCPO,X} = \gamma K_{BCPO,X} N_{BCPO} N_X \quad (10)$$

$$K_{BCPO,X} = 4\pi (R_{BCPO} + R_X)(D_{f_{BCPO}} + D_{f_X}) \quad (11)$$

where N_{BCPO} and N_X are number concentrations (m^{-3}) of BCPO and particle X computed from Eq. (6), $K_{BCPO,X}$ is the coagulation coefficient ($m^3\ s^{-1}$) that depends on particle radius (R_{BCPO} and R_X) and Brownian diffusivities ($D_{f_{BCPO}}$ and D_{f_X}), and γ (from 0.014 for 0.001 μm particles to 1.0 for 1 μm particles) is a correction factor that accounts for kinetic effects of small particles. We use geometric mean radii for R_{BCPO} and R_X, which could introduce uncertainty for particle sizes largely deviating from the mean value. We note that the resulting uncertainty in BC concentration and lifetime is likely small, because model results show that coagulation only makes a small contribution to the total BC aging rate over the globe (see Sect. 3.1) and the global BC distribution is insensitive to aerosol size distribution in this study (see Sects. 4.2 and 4.3). The hydrophobic-to-hydrophilic BC conversion rate through coagulation can be written in the form:

$$\left(\frac{dN_{BCPO}}{dt}\right)_{coag} = -\sum_{p_{j=1}}^{p_{j=6}} \gamma_{p_j} K_{BCPO,p_j} N_{p_j} N_{BCPO} \quad (12)$$

where p_j (j = 1–6) represents six types of hydrophilic particles, including sulfate-nitrate-ammonia, BCPI, hydrophilic OC, SOA, fine-mode and coarse-mode sea salt. We assume that BCPO is converted to BCPI upon coagulating with these hydrophilic aerosols. The resulting BCPO mass change per unit time ($kg\ m^{-3}\ s^{-1}$) is given by:

$$\left(\frac{dm_{BCPO}}{dt}\right)_{coag} = \frac{\pi}{6} \rho_{BCPO} D_{BCPO}^3 \exp\left(\frac{9}{2} \ln^2 \sigma_{BCPO}\right) \left(\frac{dN_{BCPO}}{dt}\right)_{coag} \quad (13)$$

2.2.1.3 Chemical oxidation

To account for the BC aging through ozone oxidation on the BC surface, we follow an experiment-based parameterization by Pöschl et al. (2001). The same parameterization

has been used in previous studies (Croft et al., 2005; Huang et al., 2013). The chemical hydrophobic-to-hydrophilic BC conversion rate (kg m^{-3} s^{-1}) can be expressed by

$$\left(\frac{dm_{BCPO}}{dt}\right)_{chem} = -k_{chem} m_{BCPO} \quad (14)$$

where k_{chem} is the reaction rate coefficient (s^{-1}) given by

$$k_{chem} = \frac{\lambda K_{\infty} K_{O_3}[O_3]}{1 + K_{O_3}[O_3] + K_{H_2O}[H_2O]} \quad (15)$$

where K_{∞} (= 0.015 s^{-1}) is the pseudo-first-order decay rate coefficient in the presence of high ozone concentrations, K_{O_3} (= 2.8×10^{-13} cm^3) and K_{H_2O} (= 2.1×10^{-17} cm^3) are the adsorption rate coefficients of O_3 and H_2O, which are a function of available adsorption sites residence time, and sticking coefficients of O_3 and H_2O on BC surface. λ (= 0.01) is the physical shielding factor that accounts for the fact that the oxidized coating material is not distributed homogenously over the BC particle surface (Croft et al., 2005). [O_3] and [H_2O] are atmospheric concentrations (molec cm^{-3}) of O_3 and H_2O, respectively.

Recent experimental studies also confirmed that BC can be aged through heterogeneous chemical oxidation by O_3 (Decesari et al., 2002; Zuberi et al., 2005) and NO_2 (Khalizov et al., 2010), which results in the formation of soluble organic compounds on BC particle surface. However, none of these recent studies have given explicit quantitative parameterizations for BC chemical aging, which can be applied in modeling studies. Moreover, experimental results presented in these studies vary substantially, suggesting that BC chemical aging process could involve large uncertainty. For this reason, the parameterization scheme developed by Pöschl et al. (2001) should be used with caution.

2.2.1.4 Total BC aging rate

We assume a linear combination of the condensation, coagulation, and chemical oxidation processes, following Croft et al. (2005) and Huang et al. (2013). The total BC

aging rate can thus be expressed in the forms:

$$\left(\frac{dm_{BCPO}}{dt}\right)_{mic} = \left(\frac{dm_{BCPO}}{dt}\right)_{cond} + \left(\frac{dm_{BCPO}}{dt}\right)_{coag} \quad (16)$$

$$\left(\frac{dm_{BCPO}}{dt}\right)_{mic+chem} = \left(\frac{dm_{BCPO}}{dt}\right)_{mic} + \left(\frac{dm_{BCPO}}{dt}\right)_{chem} \quad (17)$$

where the subscripts *mic* and *chem* represent microphysical and chemical aging, respectively. Such linear combination may overestimate BC aging rate, because these processes likely compete with each other rather than occur independently (Croft et al., 2005). However, no observational evidence is currently available to quantify interactions among these processes.

2.2.2 BC emissions

We use a global anthropogenic BC emission inventory developed by R. Wang et al. (2014) (hereinafter the PKU-BC inventory), with an annual emission of 8.5 TgC for 2008 (see Fig. S1). PKU-BC incorporates a recent global high-resolution (0.1°×0.1°) fuel combustion dataset (Wang et al., 2013) that covers 64 types of combustion based on local or national fuel statistics. The dataset significantly improves the spatial resolution of emission distribution for large countries. In addition, the inventory uses updated BC emission factors based on up-to-date measurements, particularly for developing countries (Wang et al., 2012a, b). The use of local and subnational fuel data and updated emission factors results in 70% higher global anthropogenic BC emissions than previous bottom-up inventories (4.9±0.4 TgC) (Dentener et al., 2006; Bond et al., 2007; Lamarque et al., 2010; Granier et al., 2011) yet still 20% lower than top-down estimates (Bond et al., 2013). The PKU-BC emissions are 58% higher than the global anthropogenic emissions used in our previous studies (He et al., 2014a, b). R. Wang et al. (2014) found that using PKU-BC reduces the bias in modeled surface BC concentrations by up to 25% in Asia, Africa, and Europe. However, Bond et al. (2013) pointed out that current anthropogenic

BC emission estimates are associated with large uncertainties (more than a factor of 2 across different inventories). Based on a Monte Carlo estimation, R. Wang et al. (2014) showed an uncertainty range (interquartile) of -40% to +70% for global annual anthropogenic BC emissions in PKU-BC, where errors in emission factors dominate the overall uncertainty.

We use the Global Fire Emissions Database version 3 (GFED3) (van der Werf et al., 2010) for global biomass burning emissions (see Fig. S1), which now includes small fire emissions (Randerson et al., 2012). Carbon emissions in GFED3 increase by 35% globally when small fires are included. In this study, the GFED3 emissions with a 3-hour temporal resolution are used. The uncertainty in GFED3 is ≥20% globally and highest in boreal regions and Equatorial Asia, primarily because of insufficient data on fuel load, emission factor, and burned area (van der Werf et al., 2010; Randerson et al., 2012).

2.2.3 BC deposition

Aerosol dry deposition follows a standard resistance-in-series scheme (Wesely, 1989), which depends on local surface type and meteorological conditions, as implemented by Wang et al. (1998). Wang et al. (2011) further updated aerosol dry deposition velocity over snow- and ice-covered regions for improved BC simulations in GEOS-Chem. They applied a constant value of 0.03 cm s^{-1}, within the range (0.01–0.07 cm s^{-1}) employed in previous studies (Liu et al., 2011). In the GEOS-Chem simulations presented here, dry deposition accounts for ~20% of global BC deposition, consistent with the results (17–23%) from previous studies using GEOS-Chem (He et al., 2014a; Q. Q. Wang et al., 2014) and that (21.4±17%) from the AeroCom multi-model study (Textor et al., 2006).

Liu et al. (2001) first described aerosol wet scavenging in GEOS-Chem. Wang et al. (2011) updated in the model the below-cloud scavenging parameterization for fine and

coarse aerosol modes by distinguishing between aerosol removals by snow and by rain. Different in-cloud scavenging schemes have also been applied to cold and warm clouds, with an improved areal fraction of model grids that experience precipitation (Wang et al., 2011). Following Q. Q. Wang et al. (2014), we further update in-cloud scavenging of water-soluble aerosols by accounting for homogeneous and heterogeneous freezing nucleation in cold clouds.

2.2.4 Model simulations

To investigate the effects of the microphysics-based BC aging scheme, we first conduct two GEOS-Chem BC simulations with the fixed aging (e-folding time of 1.2 days) scheme (FIX, Table 1; see also Eq. (1)) and the standard microphysics-based scheme (MP_{STD}, Table 1; see also Eq. (16)). In addition, we conduct 11 sensitivity simulations for the microphysics-based scheme to quantify the effects of chemical oxidation on BC aging and the uncertainty associated with aerosol size distribution and condensation threshold in the microphysics-based scheme. Specifically, we combine the standard microphysics-based scheme with the Pöschl et al. (2001) parameterization for chemical oxidation to examine the effects of chemical oxidation on BC aging (MP_{chem}, Table 1; see also Eq. (17)). We use geometric mean diameters of 30 nm and 90 nm for BCPO number size distribution as lower and upper bounds ($D_{BCPO}30$ and $D_{BCPO}90$, Table 1), following Bond et al. (2006), instead of 60 nm in the standard simulation (i.e., MP_{STD}). We use geometric standard deviations of 1.4 and 2.0 for BCPO number size distribution as lower and upper bounds ($SD_{BCPO}1.4$ and $SD_{BCPO}2.0$, Table 1), following Bond et al. (2006), instead of 1.8 in the standard simulation. We vary the geometric mean diameters and standard deviations of all hydrophilic particles' number size distribution in the standard simulations by ±50% (D_{PI}+50% and D_{PI}-50%, Table 1) and ±0.2 (SD_{PI}+0.2 and SD_{PI}-0.2, Table 1). We vary the condensation threshold (β in Eq. (7)) from 5% in the standard simulation to 2.5% (BETA2.5, Table 1) and to 10% (BETA10, Table 1). Model results

used for comparison with HIPPO observations are sampled along the HIPPO flight tracks.

3. Results and discussions

3.1 BC aging rate

Figure 2 shows model simulated surface-layer and zonal distributions of annual mean aging rate with the fixed (r_{fix}, calculated by Eq. 1) and microphysics-based (r_{mic}, calculated by Eq. 16) aging schemes. The maximum rates are in the surface layer over major BC source regions such as Eastern China, India, Europe, eastern United States, and tropical Africa, ranging from less than 100 ngC m^{-3} h^{-1} for the fixed scheme (Fig. 2a) to 100-500 ngC m^{-3} h^{-1} for the microphysics-based scheme (Fig. 2b). r_{mic} is 2-6 times higher than r_{fix} throughout the year over both continents and oceanic areas with heavy marine traffic (Fig. S2). This is primarily because of the strong anthropogenic emissions of SO_2, NO_X, and NH_3 in major continents and along shipping corridors in the Northern Hemisphere (Park et al., 2004) and biomass burning emissions of SOA precursors in tropical continents (Guenther et al., 2006). These emissions lead to fast BC aging through both condensation of soluble materials (i.e., H_2SO_4-HNO_3-NH_3 and SOA) and coagulation with hydrophilic particles.

Figure 3 shows the probability density function (PDF) of simulated annual mean BC e-folding aging time (τ in Eq. 1) over the globe. The first PDF peak around τ = 8 h represents the fast aging near source regions, while the second bump corresponds to τ = ~1 day, which reflects the aging over rural areas and in the middle troposphere. The third small bump is around τ = 100 h, mainly representing the very slow aging in remote regions (e.g., Polar regions and the upper troposphere). The microphysics-based scheme results in an e-folding BC aging time of 0.6–2 hours in summer and 1–3 hours in winter when averaged within the boundary layer over major anthropogenic source regions

including Eastern China, eastern United States, and Europe. These are much faster than the timescale of 1–2 days typically assumed in many global models (Chung and Seinfeld, 2002; Koch et al., 2009; He et al., 2014a). Such fast aging for anthropogenic BC has been reported in previous studies. For example, Riemer et al. (2004) used a size-resolved aerosol model to show an e-folding BC aging time of ~2-hour during the day from 250 to 1500 m above source (urban) regions for both summer and winter. Jacobson (2010) also reported a ~3-hour e-folding aging time for fossil-fuel BC based on a global size-resolved aerosol model. Shen et al. (2014) found that the e-folding aging timescale of anthropogenic BC from East Asia is several hours, based on constraints from the HIPPO observations. In addition, Akagi et al. (2012) observed that ~20% of BC ages within one hour after emission in a biomass-burning plume over California in November 2009, whereas our microphysics-based scheme shows a mean BC aging rate of 24% h^{-1} within the same region and time period. Moteki et al. (2007) measured a BC aging rate of 2.3% h^{-1} downwind of an urban area in Japan in March 2004. Though not a direct comparison, our microphysics-based scheme results in a BC aging rate of 10% h^{-1} averaged over the same region for March 2009.

r_{mic} decreases by several orders of magnitude with increasing altitude and from continents to remote oceans and the polar regions (Fig. 2). r_{fix} is a factor of 1.5–4 lower than r_{mic} below 900 hPa in the tropics and middle latitudes, but more than 5 times higher in the polar regions, remote oceans, and above 800 hPa throughout the year (Figs. S2–S3). The annual mean r_{mic} is 50% higher than r_{fix} in the middle to lower troposphere but more than fivefold lower in the middle to upper troposphere (Table 2). Because the aging rates in remote regions are vanishingly small, the difference in global BC distribution between the two aging schemes is thus dominated by the difference in the significantly larger aging rates over the source regions (see Sect. 3.3).

Figures 4a and 4b show that condensation dominates (>70%) BC aging globally, particularly in the middle to upper troposphere (500–200 hPa) and in the southern high latitudes. In contrast, the contribution from coagulation is <15% throughout much of the globe, with the exception of ~30% over Eastern China, India, and central Africa, where relatively abundant hydrophilic aerosols are available. This is primarily because hydrophilic aerosols are substantially removed by wet scavenging during the transport to remote regions, thus reducing the coagulation between hydrophobic BC and hydrophilic particles. Figures 4c and 4d show that the H_2SO_4-HNO_3-NH_3 condensation dominates (>70%) the total condensation in the northern low and middle latitudes throughout the troposphere and in the southern middle latitudes below 800 hPa. This is largely explained by strong anthropogenic emissions of SO_2 and NO_x in the Northern Hemisphere (Park et al., 2004) and global oceanic emissions of dimethylsulfide (DMS) (Lana et al., 2011). The SOA condensation, however, contributes to more than 80% of the total condensation over tropical continents dominated by biomass burning emissions and the southern extratropics above 700 hPa, where rather limited sulfuric acid is produced.

3.2 Model evaluation with HIPPO observations

Figure 5 shows the PDF of observed and simulated BC concentrations during the HIPPO measurements. Model results from the fixed aging scheme significantly overestimate BC concentrations, with a PDF peak at ~15 ng kg^{-1} (corresponding to BC in the northern extratropics) that is an order of magnitude higher than the observations. The microphysics-based aging scheme substantially reduces the discrepancy between modeled and observed PDFs, particularly at BC concentrations of <1 ng kg^{-1} and 10–50 ng kg^{-1}. The remaining model bias at extremely low BC concentrations (<0.1 ng kg^{-1}), corresponding to regions remote from combustion influence and highly influenced by tropical convection, likely reflects the inefficient BC wet scavenging in the model (Q. Q. Wang et al., 2014). Statistical analysis shows that compared with the fixed aging scheme,

the microphysics-based aging scheme reduces the percentages of modeled BC concentrations that are more than a factor of 10 and 4 higher/lower than the observations from 28% to 16% and from 53% to 37%, respectively, with a better model-observation correlation as well (Fig. 6). The median BC concentration (6.6 ng kg^{-1}) from the fixed aging scheme is biased high by a factor of four compared with the observations (1.6 ng kg^{-1}), while the microphysics-based median concentration (3.5 ng kg^{-1}) reduces the bias by a factor of two.

Figure 7 shows the median vertical profiles of BC concentration in different latitude bands from HIPPO observations and model simulations. The median in the northern extratropics (20°–90°N) is 5–10 ng kg^{-1} near the surface and decreases to <1 ng kg^{-1} above 200 hPa, while the concentration is a factor of 2–10 lower in tropical regions and Southern Hemisphere throughout the troposphere. This is because of strong BC emissions in the Northern Hemisphere and strong wet scavenging of BC during transport to the tropics and Southern Hemisphere, particularly by tropical deep convection (Q. Q. Wang et al., 2014). Model results using the fixed aging scheme generally capture the spatiotemporal pattern of BC median vertical profiles in the northern extratropics, but overestimate the magnitude by a factor of ~5 on average (Figs. 7 and S4). The largest model-observation absolute discrepancies (>20 ng kg^{-1}) are at 900–400 hPa during non-winter seasons (Fig. S4). The microphysics-based aging scheme reduces that discrepancy by 2–3 times across different altitudes in the northern extratropics, particularly at 900–300 hPa (Figs. 7 and S4). This is a result of the faster BC aging from the microphysics-based scheme over source regions in the Northern Hemisphere (Fig. 2), which increases the amount of hydrophilic BC removed by wet scavenging during the transport to the free troposphere.

In the tropics (20°S–20°N), the median BC concentration is generally less than 1 ng kg^{-1},

517 with small variations across different altitudes and seasons (Figs. 7 and S4). Model
518 results using the microphysics-based aging scheme reproduce the observed BC vertical
519 distributions in different seasons with discrepancies of <0.5 ng kg^{-1}, except for a 50%
520 underestimate in the lower troposphere (Figs. 7 and S5). This could be due to the
521 overestimate in GEOS-5 precipitation fields over the tropics (Molod et al., 2012).
522 Compared with the microphysics-based aging scheme, model results from the fixed aging
523 scheme overestimate BC concentration by more than fivefold above 800 hPa in the
524 tropics, particularly in summer and fall (Fig. S5). This is primarily because of the slow
525 BC aging over tropical source regions in the fixed aging scheme (Fig. S2), resulting in
526 insufficient BC wet removal and thus excessive BC transported to the free troposphere.
527
528 In the Southern Hemisphere (20 °–70 °S), the microphysics-based aging scheme improves
529 the modeled median BC vertical profiles by a factor of 2–4 throughout all altitudes and
530 seasons (Figs. 7 and S4) with the largest improvement at 600–200 hPa (Fig. S5),
531 compared with the fixed aging scheme. However, the microphysics-based model results
532 still overestimate the BC concentration above 300 hPa by ~3 times in the Southern
533 Hemisphere, probably due to inefficient in-cloud scavenging of BC in the model for ice
534 clouds or mixed-phase clouds at such high altitudes. However, we note that the ability of
535 BC to be ice nuclei is largely uncertain. For example, Cozic et al. (2008) suggested that
536 BC particles can act as efficient ice nuclei based on observations in mixed-phase clouds,
537 whereas Friedman et al. (2011) showed that BC particles are unlikely to serve as ice
538 nuclei efficiently in cold clouds based on laboratory experiments.
539
540 Figure 8 shows the observed and model simulated latitudinal and seasonal BC column
541 burden averaged along the HIPPO flight tracks. The lowest burden is in the tropics due to
542 strong wet scavenging by deep convection. It is two orders of magnitude lower than that
543 in the extratropical Northern Hemisphere. The burden in the Southern Hemisphere is

minimum in spring because of the wet season in the southern low latitudes (Wang and Ding, 2008), while the burden in the Northern Hemisphere is maximum during the same period when the impact of Asian outflow on the Pacific peaks (Schwarz et al., 2013). Model results using the fixed aging scheme capture the latitudinal and seasonal trend for the observations, but significantly overestimate the magnitude with a mean positive bias of 194%, particularly in the Northern Hemisphere during summer and fall, as a result of the model overestimate of BC vertical profiles in the Northern Hemisphere (Fig. 7). The microphysics-based aging scheme reduces the model overestimate at most latitudes throughout the year, with a mean positive bias of 60% and a correlation coefficient (r) of 0.85 with observations. The largest improvement from the microphysics-based scheme is in the tropics (Fig. 8), except in January.

Therefore, the microphysics-based aging scheme substantially improves BC simulations pole-to-pole over the Pacific during HIPPO, both spatially and temporally, compared with the fixed aging scheme. The remaining model-observation discrepancy, particularly in the northern extratropics and the upper troposphere, is likely a result of the uncertainty associated with BC emissions, wet scavenging, and model meteorological fields (Molod et al., 2012; Bond et al., 2013; Q. Q. Wang et al., 2014). We note that it is important to quantify the contribution of these factors to the model-observation discrepancies, which will be investigated in our future study. Additionally, the spatiotemporal variability of the observed BC concentration is significantly large within each altitude and latitude band (Fig. 7), suggesting a strong dependence of BC vertical profile on sampling location and time during the HIPPO aircraft measurements.

3.3 Global BC distribution and budget

Figures 9a and 9b show the annual mean global BC column burden from model results using the fixed and microphysics-based BC aging schemes. Both schemes result in a

similar spatial distribution of BC burden, with highest values over source regions and lowest values in the southern hemispheric oceans. However, BC burden from the microphysics-based scheme is much smaller than that from the fixed scheme globally, with the major difference over source regions throughout the year (Fig. S6). This is because the maximum enhancement of BC aging rate from the microphysics-based scheme is over source regions (Fig. 2), where there is a 20–60% increase of the hydrophilic BC fraction in total BC particles relative to the fixed aging scheme (Fig. S7). The faster hydrophobic-to-hydrophilic conversion leads to a stronger BC wet removal for the microphysics-based aging scheme. As a result, the global annual mean BC load is 0.24 mg m^{-2} in the microphysics-based scheme, consistent with the result (0.23 ± 0.07 mg m^{-2}) from the AeroCom multi-model study (Schulz et al., 2006). It is also comparable to the value (0.25 mg m^{-2}) reported by Jacobson (2010), which accounted for size-resolved aerosol microphysical processes. Bond et al. (2013) reported a much higher BC load (0.55 mg m^{-2}) based on top-down estimated BC emissions that are 70% larger than the emissions used in this study. The resulting global BC lifetime of 4.2 days from the microphysics-based scheme is within the range (3.2–9.9 days) from previous studies (Table 2).

Figures 9c and 9d show model simulated annual zonal mean BC concentration. The concentration decreases substantially from the surface in the northern middle latitudes to high altitudes and the polar regions, varying by three orders of magnitude. The concentration from the microphysics-based aging scheme is smaller than that from the fixed aging scheme at different latitudes and altitudes, with the largest difference (>400 ng m^{-3}) in the northern middle latitudes (Fig. S8). Although the microphysical aging rate is much lower than the rate from the fixed aging scheme in the middle and upper troposphere and the polar regions (Figs. 2 and S3), the faster microphysical aging over source regions dominates the aging effects on global BC distribution, resulting in a

598 substantial reduction of BC concentration globally. As a result, the fraction of global BC
599 load above 5 km is 7.3% for the microphysics-based scheme, which is close to the lower
600 bound of the range (6.1–40%) from previous studies (e.g., Schulz et al., 2006; He et al.,
601 2014b; Q. Q. Wang et al., 2014). The relatively low BC load at high altitudes in the
602 microphysics-based scheme has a significant implication for global BC radiative effects.
603 Samset et al. (2013) showed that more than 40% of global BC direct radiative forcing is
604 contributed by BC particles above 5 km, whereas this estimate has large uncertainties
605 across various models. BC particles at high altitudes could also affect the formation and
606 distribution of cirrus clouds and thus BC indirect radiative effects (e.g., Liu et al., 2009).
607
608 **4. Uncertainty analysis**
609 **4.1 Heterogeneous chemical oxidation**
610 Figure 10 shows the annual mean contribution of chemical oxidation to the total BC
611 aging rate. The contribution is 10–30% below 900 hPa over most regions at 60°S–60°N
612 latitudes, particularly at low latitudes and over source regions, due partly to the strong
613 condensation-coagulation in these areas. Additionally, the relatively high humidity and
614 low ozone concentration also contribute to less efficient chemical oxidation aging in the
615 lower troposphere and the tropics, compared with the middle troposphere and the polar
616 regions (Fig. 10b). There is efficient chemical oxidation aging over the Arctic and
617 Antarctic in the middle troposphere, where water vapor is scarce and relatively abundant
618 ozone is available. This is consistent with the conclusion from Huang et al. (2013), which
619 used the same chemical oxidation scheme and showed the lowest chemical aging rate
620 over the tropics at lower altitudes and faster aging at higher altitudes including the polar
621 regions.
622
623 Compared with the standard microphysics-based aging scheme (MP_{STD}), incorporating
624 chemical oxidation (MP_{chem}) slightly (<5%) increases the total BC aging rate at

60 °S–60 °N latitudes in the lower troposphere but more than halves the aging rate over the polar regions (Figs. 11 and 12). This is because faster BC aging over non-polar regions reduces the amount of hydrophobic BC transported to remote areas. However, the absolute aging rate over the polar regions is several orders of magnitude smaller than that in non-polar regions. Chemical oxidation aging thus has a vanishingly small (<0.5%) impact on the global annual mean BC aging rate (Table 2). It leads to only a small (<1%) reduction in BC column burden and zonal mean concentration globally (Figs. 13 and 14) as well as global BC lifetime (Table 2). Croft et al. (2005) showed a comparably small (~5%) decrease in global BC burden and lifetime when the chemical oxidation process is included, while Huang et al. (2013) found a ~10% decrease in BC burden and lifetime with the incorporation of chemical oxidation aging.

4.2 Size distribution of hydrophobic BC

Reducing the geometric mean diameter of hydrophobic BC from 60 to 30 nm ($D_{BCPO}30$) and the standard deviation from 1.8 to 1.4 ($SD_{BCPO}1.4$) increases hydrophobic BC number concentration. As a result, more hydrophobic BC particles are available for condensation-coagulation aging, leading to a 5–50% increase of condensation-induced aging rate within 60 °S–60 °N below 900 hPa (Figs. S9 and S10). The enhancement of aging rate is stronger for $SD_{BCPO}1.4$ than for $D_{BCPO}30$, suggesting that the condensation-induced aging is more sensitive to the change in geometric standard deviation than geometric mean diameter. Interestingly, the largest enhancement for both simulations is over the oceans, while only less than 10% increase occurs in the source regions. This is probably because the BC aging rate over the oceans is much smaller than that over the source regions (Fig. 2), making it more sensitive to the change in the size distribution of hydrophobic BC.

$D_{BCPO}30$ increases the coagulation-induced aging rate by up to a factor of 2 within

60 °S-60 °N near the surface (Fig. S11), particularly in source regions, whereas $SD_{BCPO}1.4$ only increases the coagulation-induced surface-layer aging rate along shipping corridors over the oceans, with up to 50% decrease in the rest of non-polar regions. In the middle to upper troposphere and the polar regions, both $D_{BCPO}30$ and $SD_{BCPO}1.4$ result in a more than 50% decrease in coagulation-induced and condensation-induced BC aging rates (Figs. S10 and S12), because of the reduction in the amount of hydrophobic BC transported to remote regions. The change in total BC aging rate shows a very similar spatial pattern with that of condensation (Figs. 11 and 12), due to the dominant role of condensation-induced aging globally. However, because of the rather low BC aging rate over the oceans and at high altitudes relative to that over source regions, the impact of hydrophobic BC size distribution on global BC distribution is dominated by the change of aging rate in source regions for both $D_{BCPO}30$ and $SD_{BCPO}1.4$, which results in less than 5% reductions in BC column burden and zonal mean concentration globally, except a 10–20% reduction in the tropics at 600–200 hPa (Figs. 13 and 14). The resulting global annual mean BC load and lifetime show negligible (<1%) increases (Table 2).

Increasing the geometric mean diameter of hydrophobic BC from 60 to 90 nm ($D_{BCPO}90$) and the standard deviation from 1.8 to 2.0 ($SD_{BCPO}2.0$) decreases hydrophobic BC number concentration. Both simulations exhibit opposite patterns of the change in BC aging rate compared with those from $D_{BCPO}30$ and $SD_{BCPO}1.4$ (Figs. S13–18), because of lower hydrophobic BC number concentrations in the former two. Nevertheless, similar to $D_{BCPO}30$ and $SD_{BCPO}1.4$, $D_{BCPO}90$ and $SD_{BCPO}2.0$ also result in less than 10% change in global BC column burden and zonal mean concentration (Figs. S19–20). We note that the observationally constrained accumulation mode BC mass size distributions for HIPPO have a geometric mean diameter of ~180 nm (Schwarz et al., 2010), which is the upper bound value used in this study for the geometric mean diameter of mass size distribution (~ 60–180 nm) converted from that of number size distribution (30–90 nm).

679

680 **4.3 Size distribution of hydrophilic aerosols**

681 Increasing the geometric mean diameters of all hydrophilic aerosols by 50% (D_{PI}+50%)
682 and the standard deviations by 0.2 (SD_{PI}+0.2) reduces the number concentration of
683 hydrophilic particles. This results in an enhanced condensation-induced aging rate due to
684 fewer hydrophilic particles competing for condensed soluble materials, but a reduced
685 coagulation-induced aging rate due to fewer hydrophilic particles available for
686 coagulating with hydrophobic BC. Both simulations show up to 50% increase in the
687 annual mean condensation-induced BC aging rate at 60°S–60°N below 900 hPa (Figs.
688 S9–10), particularly over the oceans where BC aging rate is relatively small. The faster
689 aging through condensation in the lower troposphere reduces the amount of hydrophobic
690 BC transported to higher altitudes and the polar regions, resulting in more than 50%
691 slower condensation-induced aging in remote regions. In contrast, the
692 coagulation-induced aging rate decreases globally, by 20–50% at 60°S–60°N near the
693 surface and more than 50% in elsewhere (Figs. S11 and S12). The change of total BC
694 aging rate follows the spatial pattern of the condensation-induced aging rate (Figs. 11 and
695 12). The global annual mean BC aging rate is slightly higher (~1.5%) in both D_{PI}+50 and
696 SD_{PI}+0.2. Figures 11 and 12 show that increasing geometric mean diameters and standard
697 deviations of hydrophilic particles only reduces global BC column burden and zonal
698 mean concentration by less than 10% and BC lifetime by less than 1% (Table 2).

699

700 Decreasing the geometric mean diameters of hydrophilic aerosols by 50% (D_{PI}-50%) and
701 the standard deviations by 0.2 (SD_{PI}-0.2) increases the number concentration of
702 hydrophilic particles, resulting in an opposite spatial pattern of the change in BC aging
703 rate (Figs. S13–18) than that from D_{PI}+50 and SD_{PI}+0.2. Both condensation-induced and
704 coagulation-induced aging rates are more sensitive to the decrease of geometric mean
705 diameters (D_{PI}-50%) than geometric standard deviations (SD_{PI}-0.2) globally. The

706 resulting BC concentration change is less than 10% over much of the globe, with a <2%
707 increase in global BC load and lifetime (Table 2).
708
709 **4.4 Condensation threshold**
710 The condensation-induced BC aging rate is critically dependent on the condensation
711 threshold β (see Eq. (9)), which represents the mass fraction of condensed soluble
712 materials on hydrophobic BC required for hydrophobic-to-hydrophilic BC conversion.
713 Reducing β by a factor of 2 (BETA2.5) increases the condensation-induced aging rate by
714 5–10% near source regions and by up to 50% over remote oceans at 60 °S–60 °N (Fig. S9),
715 while the condensation-induced aging rate decreases by 20–50% in the middle and upper
716 troposphere and more than 80% over the polar regions (Fig. S10), because of the reduced
717 amount of hydrophobic BC transported to remote areas. The change in total BC aging
718 rate follows the pattern of the change in condensation-induced aging rate, with major
719 increases at 60 °S–60 °N below 900 hPa (Figs. 11 and 12). This results in a decrease
720 (<20%) of BC concentration globally, particularly in the tropics at 600–200 hPa (Figs. 13
721 and 14). In contrast, doubling β (BETA10) shows the opposite spatial pattern of the
722 change in BC aging rate compared with BETA2.5 (Figs. S13 and S14), where the aging
723 rate decreases by up to 20% in the non-polar regions below 900 hPa but increases by up
724 to more than twofold at high altitudes and polar regions. The resulting global BC load
725 and lifetime, however, change by less than 2% for both BETA10 and BETA2.5 (Table 2).
726
727 There is strong spatial heterogeneity in the sensitivity of microphysical BC aging to
728 aerosol size distribution, condensation threshold, and chemical oxidation, with little
729 sensitivity over the source regions but rather large sensitivity in remote regions. However,
730 the BC aging rate in remote areas is several orders of magnitude smaller than that over
731 source regions. As a result, the global BC column burden and zonal mean concentration
732 are only slightly affected by the change in the above-mentioned factors, with less than 5%

change over much of the globe (Figs. 13 and 14). Very small changes are also seen in global BC lifetime (Table 2). Nevertheless, using a uniform aerosol size distribution and condensation threshold may not be realistic or representative, particularly on a regional scale with complex atmospheric conditions. The two-/three-moment aerosol scheme (e.g., Li et al., 2008), which predicts aerosol size distribution from simulated aerosol mass, number, and/or surface area depending on atmospheric conditions, could be a potential improvement to represent and understand BC aging, interaction with cloud, and deposition compared with the microphysical scheme developed in this study.

5. Conclusions

We have developed and examined a microphysics-based BC aging scheme that explicitly accounts for condensation and coagulation processes in GEOS-Chem global CTM. We analyzed the difference in BC aging rate between the microphysics-based scheme and a fixed aging scheme with an e-folding time of 1.2 days, followed by a systematic evaluation of BC simulations using HIPPO observations from 2009 to 2011. We further analyzed the effects of the microphysics-based aging scheme on global BC distribution and lifetime. Finally, we quantified the uncertainty associated with aerosol size distribution and condensation threshold in the microphysics-based aging scheme and the impact of heterogeneous chemical oxidation on BC aging.

In the microphysics-based BC aging scheme, we converted aerosol mass to number concentration by assuming lognormal aerosol size distributions. We computed the condensation-induced aging rate from the condensation of soluble materials onto hydrophobic BC, which converted hydrophobic to hydrophilic BC when the condensed mass reached the condensation threshold (β in Eq. (9)). We computed the coagulation-induced aging rate from the coagulation between hydrophobic BC and hydrophilic particles, assuming a hydrophobic-to-hydrophilic BC conversion upon

coagulating. This microphysics-based scheme thus incorporated an explicit microphysical representation of BC aging and retained the computational efficiency of the fixed aging scheme. The microphysical aging scheme can also be applied in other CTMs.

The microphysical aging rate was a factor of 2–6 higher than that from the fixed aging scheme in the lower troposphere over such source regions as East China, India, Europe, United States, tropical continents, and marine shipping corridors, because of strong emissions of sulfate-nitrate and SOA precursors, which resulted in faster BC aging through condensation and coagulation. The microphysical aging rate is more than fivefold lower than that from the fixed aging scheme in remote regions, where condensation and coagulation are rather weak. We found that condensation dominated (>70%) BC aging globally, particularly in the Southern Hemisphere and above 5 km, while the largest coagulation contribution (~30%) was over East China, India, and Central Africa, primarily because the hydrophilic aerosols required for coagulation were substantially removed by wet scavenging during transport to remote regions.

Compared with the fixed aging scheme, the microphysical scheme substantially reduced the discrepancy between modeled and observed probability density functions of BC concentrations during HIPPO, particularly at BC concentrations of < 1 ng kg^{-1} and 10–50 ng kg^{-1}. Model results using the fixed aging scheme overestimated BC median vertical profiles in the northern extratropics by ~5 times on average, while the microphysical scheme improved the modeled BC vertical profiles by a factor of 2–3 throughout the troposphere, particularly at 900–300 hPa. Model results using the microphysical aging scheme reproduced the observed BC vertical distribution in the tropics. In the Southern Hemisphere, the microphysical aging scheme reduced the model bias in BC vertical profiles by a factor of 2–4, with largest improvements at 600–200 hPa, compared with the fixed aging scheme. The model bias in latitudinal BC column burden along the HIPPO

787 flight tracks was reduced from +194% for the fixed aging scheme to +60% for the
788 microphysics-based scheme, with largest improvements in the tropics. The remaining
789 model-observation discrepancy for the microphysics-based simulation was likely due to
790 the uncertainty associated with BC emissions, wet scavenging, and meteorological fields
791 in the model. We note that it is also very important to evaluate BC simulations from other
792 perspectives in addition to atmospheric concentration, such as aerosol optical depth, a
793 subject requiring further investigation.
794
795 We found that the faster BC aging over the source regions from the microphysics-based
796 scheme dominated the aging effects on global BC distribution, resulting in a much lower
797 BC column burden and zonal mean concentration globally, compared with the fixed
798 aging scheme. The global annual mean BC lifetime was 4.2 days in the
799 microphysics-based scheme, where wet scavenging accounts for 80.3% of global BC
800 deposition. The resulting global BC burden was 0.25 mg m^{-2}, with 7.3% of the burden
801 above 5 km. The relatively low BC load at high altitudes had important implications on
802 the estimate of global BC radiative effects.
803
804 Furthermore, we found that BC aging rate was insensitive (<10% change) to aerosol size
805 distribution, condensation threshold, and chemical oxidation over source regions, while it
806 was the opposite (more than twofold change) in the polar regions and at high altitudes.
807 However, the BC aging rate in remote regions was orders of magnitude lower than that in
808 source regions. Thus, the global BC burden and lifetime showed little sensitivity (<5%
809 change) to the above-mentioned three factors. Nevertheless, assuming global uniform
810 aerosol size distribution and condensation threshold may not be representative or accurate,
811 particularly for regions with complex atmospheric conditions. Further improvements
812 require the incorporation of a dynamic size-resolved microphysical aging scheme.
813

Acknowledgements

This work is funded by NASA grants NNX09AF07G and NNX08AF64G from the Atmospheric Chemistry Modeling and Analysis Program (ACMAP) and by the NSF grants AGS-0946315 and AGS-1523296. We acknowledge the free use of HIPPO data. We thank all the contributors during the HIPPO campaigns and all the contributors to the development of PKU-BC inventory. We thank Rong Wang, Fangqun Yu, Peter Adams, David Fahey, and Jiachen Zhang for helpful discussions.

References

Akagi, S. K., Craven, J. S., Taylor, J. W., McMeeking, G. R., Yokelson, R. J., Burling, I. R., Urbanski, S. P., Wold, C. E., Seinfeld, J. H., Coe, H., Alvarado, M. J., and Weise, D. R.: Evolution of trace gases and particles emitted by a chaparral fire in California, Atmos. Chem. Phys., 12, 1397-1421, doi:10.5194/acp-12-1397-2012, 2012.

Alexander, B., Park, R. J., Jacob, D. J., Li, Q. B., Yantosca, R. M., Savarino, J., Lee, C. C. W., and Thiemens, M. H.: Sulfate formation in sea-salt aerosols: Constraints from oxygen isotopes, J. Geophys. Res.-Atmos., 110, D10307, doi:10.1029/2004jd005659, 2005.

Aquila, V., Hendricks, J., Lauer, A., Riemer, N., Vogel, H., Baumgardner, D., Minikin, A., Petzold, A., Schwarz, J. P., Spackman, J. R., Weinzierl, B., Righi, M., and Dall'Amico, M.: MADE-in: a new aerosol microphysics submodel for global simulation of insoluble particles and their mixing state, Geosci. Model Dev., 4, 325–355, doi:10.5194/gmd-4-325-2011, 2011.

Bond, T. C., Habib, G., and Bergstrom, R. W.: Limitations in the enhancement of visible light absorption due to mixing state, J. Geophys. Res.-Atmos., 111, D20211, doi:10.1029/2006jd007315, 2006.

Bond, T. C., Bhardwaj, E., Dong, R., Jogani, R., Jung, S. K., Roden, C., Streets, D. G., and Trautmann, N. M.: Historical emissions of black and organic carbon aerosol from energy-related combustion, 1850-2000, Global Biogeochem. Cy., 21, Gb2018, doi:10.1029/2006gb002840, 2007.

841 Bond, T. C., Doherty, S. J., Fahey, D. W., Forster, P. M., Berntsen, T., DeAngelo, B. J., Flanner, M. G.,
842 Ghan, S., Karcher, B., Koch, D., Kinne, S., Kondo, Y., Quinn, P. K., Sarofim, M. C., Schultz, M.
843 G., Schulz, M., Venkataraman, C., Zhang, H., Zhang, S., Bellouin, N., Guttikunda, S. K., Hopke,
844 P. K., Jacobson, M. Z., Kaiser, J. W., Klimont, Z., Lohmann, U., Schwarz, J. P., Shindell, D.,
845 Storelvmo, T., Warren, S. G., and Zender, C. S.: Bounding the role of black carbon in the climate
846 system: A scientific assessment, J. Geophys. Res.-Atmos., 118, 5380-5552,
847 doi:10.1002/jgrd.50171, 2013.
848 Chung, S. H. and Seinfeld, J. H.: Global distribution and climate forcing of carbonaceous aerosols, J.
849 Geophys. Res.-Atmos., 107, 4407, doi:10.1029/2001JD001397, 2002.
850 Cooke, W. F., Liousse, C., Cachier, H., and Feichter, J.: Construction of a 1 degrees x 1 degrees fossil
851 fuel emission data set for carbonaceous aerosol and implementation and radiative impact in the
852 ECHAM4 model, J. Geophys. Res.-Atmos., 104, 22137–22162, doi:10.1029/1999jd900187,
853 1999.
854 Cozic, J., Mertes, S., Verheggen, B., Cziczo, D. J., Gallavardin, S. J., Walter, S., Baltensperger, U., and
855 Weingartner, E.: Black carbon enrichment in atmospheric ice particle residuals observed in lower
856 tropospheric mixed phase clouds, J. Geophys. Res.-Atmos., 113, D15209,
857 doi:10.1029/2007jd009266, 2008.
858 Croft, B., Lohmann, U., and von Salzen, K.: Black carbon ageing in the Canadian Centre for Climate
859 modelling and analysis atmospheric general circulation model, Atmos. Chem. Phys., 5,
860 1931–1949, doi:10.5194/acp-5-1931-2005, 2005.
861 Dahneke, B.: Simple kinetic theory of Brownian diffusion in vapors and aerosols, in Theory of
862 Dispersed Multiphase Flow, R. E. Meyer, ed., Academic Press, New York, 97-133, 1983.
863 Decesari, S., Facchini, M. C., Matta, E., Mircea, M., Fuzzi, S., Chughtai, A. R., and Smith, D. M.:
864 Water soluble organic compounds formed by oxidation of soot, Atmos. Environ., 36, 1827-1832,
865 doi:10.1016/S1352-2310(02)00141-3, 2002.
866 Dentener, F., Kinne, S., Bond, T., Boucher, O., Cofala, J., Generoso, S., Ginoux, P., Gong, S.,
867 Hoelzemann, J. J., Ito, A., Marelli, L., Penner, J. E., Putaud, J.-P., Textor, C., Schulz, M., van der

868 Werf, G. R., and Wilson, J.: Emissions of primary aerosol and precursor gases in the years 2000
869 and 1750 prescribed datasets for AeroCom, Atmos. Chem. Phys., 6, 4321–4344,
870 doi:10.5194/acp-6-4321-2006, 2006.
871 Fairlie, T. D., Jacob, D. J., and Park, R. J.: The impact of transpacific transport of mineral dust in the
872 United States, Atmos. Environ., 41, 1251-1266, doi:10.1016/j.atmosenv.2006.09.048, 2007.
873 Friedman, B., Kulkarni, G., Beranek, J., Zelenyuk, A., Thornton, J. A., and Cziczo, D. J.: Ice
874 nucleation and droplet formation by bare and coated soot particles, J. Geophys. Res.-Atmos., 116,
875 D17203, doi:10.1029/2011jd015999, 2011.
876 Guenther, A., Karl, T., Harley, P., Wiedinmyer, C., Palmer, P. I., and Geron, C.: Estimates of global
877 terrestrial isoprene emissions using MEGAN (Model of Emissions of Gases and Aerosols from
878 Nature), Atmos. Chem. Phys., 6, 3181-3210, 2006.
879 Granier, C., Bessagnet, B., Bond, T., D'Angiola, A., van der Gon, H. D., Frost, G. J., Heil, A., Kaiser, J.
880 W., Kinne, S., Klimont, Z., Kloster, S., Lamarque, J. F., Liousse, C., Masui, T., Meleux, F.,
881 Mieville, A., Ohara, T., Raut, J. C., Riahi, K., Schultz, M. G., Smith, S. J., Thompson, A., van
882 Aardenne, J., van der Werf, G. R., and van Vuuren, D. P.: Evolution of anthropogenic and
883 biomass burning emissions of air pollutants at global and regional scales during the 1980-2010
884 period, Climatic Change, 109, 163-190, doi:10.1007/s10584-011-0154-1, 2011.
885 He, C., Li, Q. B., Liou, K. N., Zhang, J., Qi, L., Mao, Y., Gao, M., Lu, Z., Streets, D. G., Zhang, Q.,
886 Sarin, M. M., and Ram, K.: A global 3-D CTM evaluation of black carbon in the Tibetan Plateau,
887 Atmos. Chem. Phys., 14, 7091-7112, doi:10.5194/acp-14-7091-2014, 2014a.
888 He, C., Li, Q. B., Liou, K. N., Takano, Y., Gu, Y., Qi, L., Mao, Y. H., and Leung, L. R.: Black carbon
889 radiative forcing over the Tibetan Plateau, Geophys. Res. Lett., 41, 7806-7813,
890 doi:10.1002/2014gl062191, 2014b.
891 He, C., Liou, K.-N., Takano, Y., Zhang, R., Levy Zamora, M., Yang, P., Li, Q., and Leung, L. R.:
892 Variation of the radiative properties during black carbon aging: theoretical and experimental
893 intercomparison, Atmos. Chem. Phys., 15, 11967-11980, doi:10.5194/acp-15-11967-2015, 2015.
894 Huang, Y., Wu, S., Dubey, M. K., and French, N. H. F.: Impact of aging mechanism on model

simulated carbonaceous aerosols, Atmos. Chem. Phys., 13, 6329–6343, doi:10.5194/acp-13-6329-2013, 2013.

Jacobson, M. Z.: Short-term effects of controlling fossil-fuel soot, biofuel soot and gases, and methane on climate, Arctic ice, and air pollution health, J. Geophys. Res.-Atmos., 115, D14209, doi:10.1029/2009jd013795, 2010.

Jacobson, M. Z.: Effects of biomass burning on climate, accounting for heat and moisture fluxes, black and brown carbon, and cloud absorption effects, J. Geophys. Res. Atmos., 119, 8980–9002, doi:10.1002/2014JD021861, 2014.

Johnson, K. S., Zuberi, B., Molina, L. T., Molina, M. J., Iedema, M. J., Cowin, J. P., Gaspar, D. J., Wang, C., and Laskin, A.: Processing of soot in an urban environment: case study from the Mexico City Metropolitan Area, Atmos. Chem. Phys., 5, 3033-3043, 2005.

Khalizov, A. F., Cruz-Quinones, M., and Zhang, R. Y.: Heterogeneous Reaction of NO2 on Fresh and Coated Soot Surfaces, J. Phys. Chem. A, 114, 7516-7524, doi:10.1021/Jp1021938, 2010.

Koch, D., Schulz, M., Kinne, S., McNaughton, C., Spackman, J. R., Balkanski, Y., Bauer, S., Berntsen, T., Bond, T. C., Boucher, O., Chin, M., Clarke, A., De Luca, N., Dentener, F., Diehl, T., Dubovik, O., Easter, R., Fahey, D. W., Feichter, J., Fillmore, D., Freitag, S., Ghan, S., Ginoux, P., Gong, S., Horowitz, L., Iversen, T., Kirkevag, A., Klimont, Z., Kondo, Y., Krol, M., Liu, X., Miller, R., Montanaro, V., Moteki, N., Myhre, G., Penner, J. E., Perlwitz, J., Pitari, G., Reddy, S., Sahu, L., Sakamoto, H., Schuster, G., Schwarz, J. P., Seland, O., Stier, P., Takegawa, N., Takemura, T., Textor, C., van Aardenne, J. A., and Zhao, Y.: Evaluation of black carbon estimations in global aerosol models, Atmos. Chem. Phys., 9, 9001-9026, 2009.

Koepke, P., Hess, M., Schult, I., and Shettle, E. P.: Global Aerosol Data Set, Report No. 243, Max-Planck-Institut fur Meteorologie, Hamburg, ISSN 0937-1060, 1997.

Kondo, Y., Sahu, L., Moteki, N., Khan, F., Takegawa, N., Liu, X., Koike, M., and Miyakawa, T.: Consistency and traceability of black carbon measurements made by laser-induced incandescence, thermal-optical transmittance, and filter-based photo-absorption techniques, Aero. Sci. Technol., 45, 295-312, 2011.

922 Lamarque, J. F., Bond, T. C., Eyring, V., Granier, C., Heil, A., Klimont, Z., Lee, D., Liousse, C.,
923 Mieville, A., Owen, B., Schultz, M. G., Shindell, D., Smith, S. J., Stehfest, E., Van Aardenne, J.,
924 Cooper, O. R., Kainuma, M., Mahowald, N., McConnell, J. R., Naik, V., Riahi, K., and van
925 Vuuren, D. P.: Historical (1850-2000) gridded anthropogenic and biomass burning emissions of
926 reactive gases and aerosols: methodology and application, Atmos. Chem. Phys., 10, 7017-7039,
927 2010.
928 Lana, A., Bell, T. G., Simo, R., Vallina, S. M., Ballabrera-Poy, J., Kettle, A. J., Dachs, J., Bopp, L.,
929 Saltzman, E. S., Stefels, J., Johnson, J. E., and Liss, P. S.: An updated climatology of surface
930 dimethlysulfide concentrations and emission fluxes in the global ocean, Global Biogeochem. Cy.,
931 25, Gb1004, doi:10.1029/2010gb003850, 2011.
932 Li, G. H., Wang, Y., and Zhang, R. Y.: Implementation of a two-moment bulk microphysics scheme to
933 the WRF model to investigate aerosol-cloud interaction, J. Geophys. Res.-Atmos., 113, D15211,
934 doi:10.1029/2007jd009361, 2008.
935 Li, K., Liao, H., Mao, Y., and Ridley, D. A.: Source sector and region contributions to concentration
936 and direct radiative forcing of black carbon in China, Atmos. Environ.,
937 doi:10.1016/j.atmosenv.2015.06.014, 2015.
938 Liao, H., Henze, D. K., Seinfeld, J. H., Wu, S. L., and Mickley, L. J.: Biogenic secondary organic
939 aerosol over the United States: Comparison of climatological simulations with observations, J.
940 Geophys. Res.-Atmos., 112, D06201, doi:10.1029/2006jd007813, 2007.
941 Liou, K. N., Takano, Y., He, C., Yang, P., Leung, L. R., Gu, Y., and Lee, W. L.: Stochastic
942 parameterization for light absorption by internally mixed BC/dust in snow grains for application
943 to climate models, J. Geophys. Res.-Atmos., 119, 7616-7632, doi:10.1002/2014jd021665, 2014.
944 Liu, H. Y., Jacob, D. J., Bey, I., and Yantosca, R. M.: Constraints from Pb-210 and Be-7 on wet
945 deposition and transport in a global three-dimensional chemical tracer model driven by
946 assimilated meteorological fields, J. Geophys. Res.-Atmos., 106, 12109–12128,
947 doi:10.1029/2000jd900839, 2001.
948 Liu, J. F., Fan, S. M., Horowitz, L. W., and Levy, H.: Evaluation of factors controlling long-range

transport of black carbon to the Arctic, J. Geophys. Res.-Atmos., 116, D04307, doi:10.1029/2010jd015145, 2011.

Liu, X. H., Penner, J. E., and Wang, M. H.: Influence of anthropogenic sulfate and black carbon on upper tropospheric clouds in the NCAR CAM3 model coupled to the IMPACT global aerosol model, J. Geophys. Res.-Atmos., 114, D03204, doi:10.1029/2008jd010492, 2009.

Moffet, R. C., and Prather, K. A.: In-situ measurements of the mixing state and optical properties of soot with implications for radiative forcing estimates, P. Natl. Acad. Sci. USA, 106, 11872-11877, doi:10.1073/pnas.0900040106, 2009.

Molod, A., Takacs, L., Suarez, M., Bacmeister, J., Song, I.-S., and Eichmann, A.: The GEOS-5 Atmospheric General Circulation Model: Mean Climate and Development from MERRA to Fortuna. NASA Technical Report Series on Global Modeling and Data Assimilation, NASA TM—2012-104606, Vol. 28, 117 pp, 2012.

Moteki, N., Kondo, Y., Miyazaki, Y., Takegawa, N., Komazaki, Y., Kurata, G., Shirai, T., Blake, D. R., Miyakawa, T., and Koike, M.: Evolution of mixing state of black carbon particles: Aircraft measurements over the western Pacific in March 2004, Geophys. Res. Lett., 34, L11803, doi:10.1029/2006gl028943, 2007.

Oshima, N., and Koike, M.: Development of a parameterization of black carbon aging for use in general circulation models, Geosci. Model Dev., 6, 263-282, doi:10.5194/gmd-6-263-2013, 2013.

Park, R. J., Jacob, D. J., Chin, M., and Martin, R. V.: Sources of carbonaceous aerosols over the United States and implications for natural visibility, J. Geophys. Res.-Atmos., 108, 4355, doi:10.1029/2002jd003190, 2003.

Park, R. J., Jacob, D. J., Field, B. D., Yantosca, R. M., and Chin, M.: Natural and transboundary pollution influences on sulfate-nitrate-ammonium aerosols in the United States: Implications for policy, J. Geophys. Res.-Atmos., 109, D15204, doi:10.1029/2003jd004473, 2004.

Park, R. J., Jacob, D. J., Palmer, P. I., Clarke, A. D., Weber, R. J., Zondlo, M. A., Eisele, F. L., Bandy, A. R., Thornton, D. C., Sachse, G. W., and Bond, T. C.: Export efficiency of black carbon aerosol in continental outflow: Global implications, J. Geophys. Res.-Atmos., 110, D11205,

doi:10.1029/2004jd005432, 2005.

Painter, T. H., Flanner, M. G., Kaser, G., Marzeion, B., VanCuren, R. A., and Abdalati, W.: End of the Little Ice Age in the Alps forced by industrial black carbon, P. Natl. Acad. Sci. USA, 110, 15216-15221, doi:10.1073/pnas.1302570110, 2013.

Pöschl, U., Letzel, T., Schauer, C., and Niessner, R.: Interaction of ozone and water vapor with spark discharge soot aerosol particles coated with benzo[a]pyrene: O3 and H2O adsorption, benzo[a]pyrene degradation, and atmospheric implications, J. Phys. Chem. A, 105, 4029–4041, doi:10.1021/jp004137n, 2001.

Prenni, A. J., Petters, M. D., Kreidenweis, S. M., DeMott, P. J., and Ziemann, P. J.: Cloud droplet activation of secondary organic aerosol, J. Geophys. Res.-Atmos., 112, D10223, doi:10.1029/2006jd007963, 2007.

Ramanathan, V. and Carmichael, G.: Global and regional climate changes due to black carbon, Nat. Geosci., 1, 221–227, doi:10.1038/ngeo156, 2008.

Randerson, J. T., Chen, Y., van der Werf, G. R., Rogers, B. M., and Morton, D. C.: Global burned area and biomass burning emissions from small fires, J. Geophys. Res.-Biogeo., 117, G04012, doi:10.1029/2012jg002128, 2012.

Riemer, N., Vogel, H., and Vogel, B.: Soot aging time scales in polluted regions during day and night, Atmos. Chem. Phys., 4, 1885–1893, doi:10.5194/acp-4-1885-2004, 2004.

Samset, B. H., Myhre, G., Schulz, M., Balkanski, Y., Bauer, S., Berntsen, T. K., Bian, H., Bellouin, N., Diehl, T., Easter, R. C., Ghan, S. J., Iversen, T., Kinne, S., Kirkevag, A., Lamarque, J. F., Lin, G., Liu, X., Penner, J. E., Seland, O., Skeie, R. B., Stier, P., Takemura, T., Tsigaridis, K., and Zhang, K.: Black carbon vertical profiles strongly affect its radiative forcing uncertainty, Atmos. Chem. Phys., 13, 2423-2434, doi:10.5194/acp-13-2423-2013, 2013.

Scarnato, B. V., Vahidinia, S., Richard, D. T., and Kirchstetter, T. W.: Effects of internal mixing and aggregate morphology on optical properties of black carbon using a discrete dipole approximation model, Atmos. Chem. Phys., 13, 5089-5101, doi:10.5194/acp-13-5089-2013, 2013.

1003 Schwarz, J. P., Gao, R. S., Spackman, J. R., Watts, L. A., Thomson, D. S., Fahey, D. W., Ryerson, T. B.,
1004 Peischl, J., Holloway, J. S., Trainer, M., Frost, G. J., Baynard, T., Lack, D. A., de Gouw, J. A.,
1005 Warneke, C., and Del Negro, L. A.: Measurement of the mixing state, mass, and optical size of
1006 individual black carbon particles in urban and biomass burning emissions, Geophys. Res. Lett.,
1007 35, L13810, doi:10.1029/2008gl033968, 2008.
1008 Schwarz, J. P., Spackman, J. R., Gao, R. S., Watts, L. A., Stier, P., Schulz, M., Davis, S. M., Wofsy, S.
1009 C., and Fahey, D. W.: Global-scale black carbon profiles observed in the remote atmosphere and
1010 compared to models, Geophys. Res. Lett., 37, L18812, doi:10.1029/2010gl044372, 2010.
1011 Schwarz, J. P., Samset, B. H., Perring, A. E., Spackman, J. R., Gao, R. S., Stier, P., Schulz, M., Moore,
1012 F. L., Ray, E. A., and Fahey, D. W.: Global-scale seasonally resolved black carbon vertical
1013 profiles over the Pacific, Geophys. Res. Lett., 40, 5542-5547, doi:10.1002/2013gl057775, 2013.
1014 Seinfeld, J. H., and S. N. Pandis, Atmospheric Chemistry and Physics, From Air Pollution to Climate
1015 Change, 2nd ed., John Wiley, Hoboken, N. J., 400–610, 2006.
1016 Shen, Z., Liu, J., Horowitz, L. W., Henze, D. K., Fan, S., H., Levy II, Mauzerall, D. L., Lin, J.-T., and
1017 Tao, S.: Analysis of transpacific transport of black carbon during HIPPO-3: implications for
1018 black carbon aging, Atmos. Chem. Phys., 14, 6315-6327, doi:10.5194/acp-14-6315-2014, 2014.
1019 Schulz, M., Textor, C., Kinne, S., Balkanski, Y., Bauer, S., Berntsen, T., Berglen, T., Boucher, O.,
1020 Dentener, F., Guibert, S., Isaksen, I. S. A., Iversen, T., Koch, D., Kirkevag, A., Liu, X.,
1021 Montanaro, V., Myhre, G., Penner, J. E., Pitari, G., Reddy, S., Seland, O., Stier, P., and Takemura,
1022 T.: Radiative forcing by aerosols as derived from the AeroCom present-day and pre-industrial
1023 simulations, Atmos. Chem. Phys., 6, 5225-5246, 2006.
1024 Textor, C., Schulz, M., Guibert, S., Kinne, S., Balkanski, Y., Bauer, S., Berntsen, T., Berglen, T.,
1025 Boucher, O., Chin, M., Dentener, F., Diehl, T., Easter, R., Feichter, H., Fillmore, D., Ghan, S.,
1026 Ginoux, P., Gong, S., Grini, A., Hendricks, J., Horowitz, L., Huang, P., Isaksen, I., Iversen, I.,
1027 Kloster, S., Koch, D., Kirkevåg, A., Kristjansson, J. E., Krol, M., Lauer, A., Lamarque, J. F., Liu,
1028 X., Montanaro, V., Myhre, G., Penner, J., Pitari, G., Reddy, S., Seland, Ø., Stier, P., Takemura, T.,
1029 and Tie, X.: Analysis and quantification of the diversities of aerosol life cycles within AeroCom,

1030 Atmos. Chem. Phys., 6, 1777–1813, doi:10.5194/acp-6-1777-2006, 2006.
1031 van der Werf, G. R., Randerson, J. T., Giglio, L., Collatz, G. J., Mu, M., Kasibhatla, P. S., Morton, D.
1032 C., DeFries, R. S., Jin, Y., and van Leeuwen, T. T.: Global fire emissions and the contribution of
1033 deforestation, savanna, forest, agricultural, and peat fires (1997–2009), Atmos. Chem. Phys., 10,
1034 11707-11735, doi:10.5194/acp-10-11707-2010, 2010.
1035 Wang, B., and Ding, Q. H.: Global monsoon: Dominant mode of annual variation in the tropics,
1036 Dynam. Atmos. Oceans, 44, 165-183, doi:10.1016/j.dynatmoce.2007.05.002, 2008.
1037 Wang, R., Tao, S., Wang, W. T., Liu, J. F., Shen, H. Z., Shen, G. F., Wang, B., Liu, X. P., Li, W., Huang,
1038 Y., Zhang, Y. Y., Lu, Y., Chen, H., Chen, Y. C., Wang, C., Zhu, D., Wang, X. L., Li, B. G., Liu, W.
1039 X., and Ma, J. M.: Black Carbon Emissions in China from 1949 to 2050, Environ. Sci. Technol.,
1040 46, 7595–7603, doi:10.1021/Es3003684, 2012a.
1041 Wang, R., Tao, S., Shen, H. Z., Wang, X. L., Li, B. G., Shen, G. F., Wang, B., Li, W., Liu, X. P., Huang,
1042 Y., Zhang, Y. Y., Lu, Y., and Ouyang, H. L.: Global Emission of Black Carbon from Motor
1043 Vehicles from 1960 to 2006, Environ. Sci. Technol., 46, 1278-1284, doi:10.1021/es2032218,
1044 2012b.
1045 Wang, R., Tao, S., Ciais, P., Shen, H. Z., Huang, Y., Chen, H., Shen, G. F., Wang, B., Li, W., Zhang, Y.
1046 Y., Lu, Y., Zhu, D., Chen, Y. C., Liu, X. P., Wang, W. T., Wang, X. L., Liu, W. X., Li, B. G., and
1047 Piao, S. L.: High-resolution mapping of combustion processes and implications for CO2
1048 emissions, Atmos. Chem. Phys., 13, 5189-5203, doi:10.5194/acp-13-5189-2013, 2013.
1049 Wang, R., Tao, S., Balkanski, Y., Ciais, P., Boucher, O., Liu, J. F., Piao, S. L., Shen, H. Z., Vuolo, M.
1050 R., Valari, M., Chen, H., Chen, Y. C., Cozic, A., Huang, Y., Li, B. G., Li, W., Shen, G. F., Wang,
1051 B., and Zhang, Y. Y.: Exposure to ambient black carbon derived from a unique inventory and
1052 high-resolution model, P. Natl. Acad. Sci. USA., 111, 2459–2463, doi:10.1073/pnas.1318763111,
1053 2014b.
1054 Wang, Q., Jacob, D. J., Fisher, J. A., Mao, J., Leibensperger, E. M., Carouge, C. C., Le Sager, P.,
1055 Kondo, Y., Jimenez, J. L., Cubison, M. J., and Doherty, S. J.: Sources of carbonaceous aerosols
1056 and deposited black carbon in the Arctic in winter-spring: implications for radiative forcing,

1057 Atmos. Chem. Phys., 11, 12453–12473, doi:10.5194/acp-11-12453-2011, 2011.
1058 Wang, Q. Q., Jacob, D. J., Spackman, J. R., Perring, A. E., Schwarz, J. P., Moteki, N., Marais, E. A.,
1059 Ge, C., Wang, J., and Barrett, S. R. H.: Global budget and radiative forcing of black carbon
1060 aerosol: Constraints from pole-to-pole (HIPPO) observations across the Pacific, J. Geophys.
1061 Res.-Atmos., 119, 195-206, doi:10.1002/2013jd020824, 2014a.
1062 Wang, Y. H., Jacob, D. J., and Logan, J. A.: Global simulation of tropospheric O3-NOx-hydrocarbon
1063 chemistry 1. Model formulation, J. Geophys. Res.-Atmos., 103, 10713–10725,
1064 doi:10.1029/98jd00158, 1998.
1065 Weingartner, E., Burtscher, H., and Baltensperger, H.: Hygroscopic properties of carbon and diesel
1066 soot particles, Atmos. Environ., 31, 2311–2327, 1997.
1067 Wesely, M. L.: Parameterization of Surface Resistances to Gaseous Dry Deposition in Regional-Scale
1068 Numerical Models, Atmos. Environ., 23, 1293–1304, doi:10.1016/0004-6981(89)90153-4, 1989.
1069 Willis, M. D., Healy, R. M., Riemer, N., West, M., Wang, J. M., Jeong, C.-H., Wenger, J. C., Evans, G.
1070 J., Abbatt, J. P. D., and Lee, A. K. Y.: Quantification of black carbon mixing state from traffic:
1071 implications for aerosol optical properties, Atmos. Chem. Phys. Discuss., 15, 33555-33582,
1072 doi:10.5194/acpd-15-33555-2015, 2015.
1073 Wofsy, S. C., Team, H. S., Team, C. M., and Team, S.: HIAPER Pole-to-Pole Observations (HIPPO):
1074 fine-grained, global-scale measurements of climatically important atmospheric gases and
1075 aerosols, Philos. T. R. Soc. A, 369, 2073-2086, doi:10.1098/rsta.2010.0313, 2011.
1076 Yu, F. and Luo, G.: Simulation of particle size distribution with a global aerosol model: contribution of
1077 nucleation to aerosol and CCN number concentrations, Atmos. Chem. Phys., 9, 7691–7710,
1078 doi:10.5194/acp-9-7691-2009, 2009.
1079 Zhang, J., Liu, J., Tao, S., and Ban-Weiss, G. A.: Long-range transport of black carbon to the Pacific
1080 Ocean and its dependence on aging timescale, Atmos. Chem. Phys., 15, 11521-11535,
1081 doi:10.5194/acp-15-11521-2015, 2015.
1082 Zhang, R. Y., Khalizov, A. F., Pagels, J., Zhang, D., Xue, H. X., and McMurry, P. H.: Variability in
1083 morphology, hygroscopicity, and optical properties of soot aerosols during atmospheric

1084 processing, P. Natl. Acad. Sci. USA, 105, 10291-10296, doi:10.1073/pnas.0804860105, 2008.
1085 Zuberi, B., Johnson, K. S., Aleks, G. K., Molina, L. T., and Laskin, A.: Hydrophilic properties of aged
1086 soot, Geophys. Res. Lett., 32, L01807, doi:10.1029/2004gl021496, 2005.
1087

Table 1. Key aging parameters used in GEOS-Chem simulations of BC.

Simulations		Hydrophobic[a]		Hydrophilic[a]		Condensation threshold (β)[b]
		D_p (nm)	σ_p	D_p (nm)	σ_p	
Fixed aging (FIX)		e-folding BC aging time τ_{fix} = 1.2 days				
Standard Microphysics-based (MP_{STD})[c]		D_{BC} = 60 D_{OC} = 60	σ_{BC} = 1.8 σ_{OC} = 1.8	D_{BC} = 150 D_{OC} = 150 D_{sulf} = 150 D_{fss} = 200 D_{css} = 800	σ_{BC} = 1.8 σ_{OC} = 1.8 σ_{sulf} = 1.6 σ_{fss} = 1.5 σ_{css} = 1.8	5% of hydrophobic BC mass
Sensitivity simulations	$D_{BCPO}30$	Hydrophobic D_{BC} = 30 nm[d]				
	$D_{BCPO}90$	Hydrophobic D_{BC} = 90 nm[d]				
	$SD_{BCPO}1.4$	Hydrophobic σ_{BC} = 1.4[d]				
	$SD_{BCPO}2.0$	Hydrophobic σ_{BC} = 2.0[d]				
	D_{PI}+50%	All hydrophilic particles D_p increased by 50%				
	D_{PI}-50%	All hydrophilic particles D_p decreased by 50%				
	SD_{PI}+0.2	All hydrophilic particles σ_p increased by 0.2				
	SD_{PI}-0.2	All hydrophilic particles σ_p decreased by 0.2				
	BETA2.5	β = 2.5%				
	BETA10	β = 10%				
	MP_{chem}	Standard microphysics-based scheme with chemical oxidation parameterization from Poschl et al. (2001)				

[a] D_p and σ_p are geometric mean diameter and geometric standard deviation for particle number size distribution, respectively.

[b] Condensation threshold (β in Eq. (7)) represents the mass fraction of condensed soluble materials on hydrophobic BC required for hydrophobic-to-hydrophilic BC conversion. A value of 5% is used in the standard microphysics-based scheme following Riemer et al. (2004).

[c] Geometric mean diameters (D_p)and standard deviations (σ_p) are followling Dentener et al. (2006) and Yu and Luo (2009) for hydrophobic and hydrophilic BC and OC, and the Global Aerosol Dataset (GADS) (Koepke et al., 1997) for sulfate-nitrate-ammonia ("sulf"), fine-mode sea salt ("fss"), and coarse-mode sea salt ("css"). SOA is treated as hydrophilic OC.

[d] Lower and upper bounds of geometric mean diameters (30 nm and 90 nm) and standard deviations (1.4 and 2.0) for hydrophobic BC are following Bond et al. (2006).

Table 2. GEOS-Chem simulated global annual mean BC budget.

References		BC aging rate (ngC m^{-3} h^{-1})			Emissions (Tg yr^{-1})[c]	Lifetime (day)	Loading (mg m^{-2})	Loading above 5 km (%)	Wet deposition (%)	Hydrophilic fraction (%)
		< 5 km	> 5 km	mean						
This study	FIX	0.378	0.005	0.221	10.8	13.7	0.795	26.2	78.9	85.8
	MP_{STD}	0.560	< 0.001	0.324		4.21	0.244	7.32	80.3	98.8
	MP_{chem}	0.561		0.325		4.21	0.244	7.31	80.3	98.9
	$D_{BCPO}30$	0.570		0.330		4.18	0.242	7.16	80.2	99.3
	$D_{BCPO}90$	0.551		0.319		4.25	0.246	7.53	80.3	98.1
	$SD_{BCPO}1.4$	0.571		0.331		4.18	0.242	7.14	80.2	99.4
	$SD_{BCPO}2.0$	0.550		0.319		4.25	0.246	7.55	80.3	98.1
	D_{PI}+50%	0.568		0.329		4.19	0.243	7.19	80.3	99.2
	D_{PI}-50%	0.548		0.317		4.27	0.247	7.68	80.2	97.8
	SD_{PI}+0.2	0.567		0.328		4.19	0.243	7.20	80.3	99.2
	SD_{PI}-0.2	0.552		0.320		4.24	0.246	7.50	80.3	98.2
	BETA2.5	0.569		0.330		4.19	0.242	7.17	80.3	99.3
	BETA10	0.547		0.317		4.27	0.247	7.65	80.2	97.7
He et al. (2014a, b)		Fixed aging (τ = 1.2 days)			8.1	6.6	0.29	18	83	-
Q. Q. Wang et al. (2014)		Fixed aging (τ = 1.2 days)			6.5	4.2	0.15	8.7	77	-
Bond et al. (2013)[a]		Model ensemble mean			17	6.1	0.55	-	-	-
Jacobson (2012)		Aging microphysics			9.3	3.2	0.18	-	94	-
Chung et al. (2012)		Fixed aging			6.3	5.5	0.19	-	-	-
Jacobson (2010)		Aging microphysics			4.7	9.9	0.25	-	92	-
Schulz et al. (2006)[b]		Model ensemble mean			6.3	6.8 ±1.8	0.23 ±0.07	21 ±11	-	-

[a]Based on AeroCom Phase I simulations after scaling to match AERONET BC absorption optical depth (AAOD).

[b]Mean and standard deviations for eight models from AeroCom Phase I simulations. All AeroCom models use the same emissions.

[c]Global total BC emissions including anthropogenic and biomass burning sources.

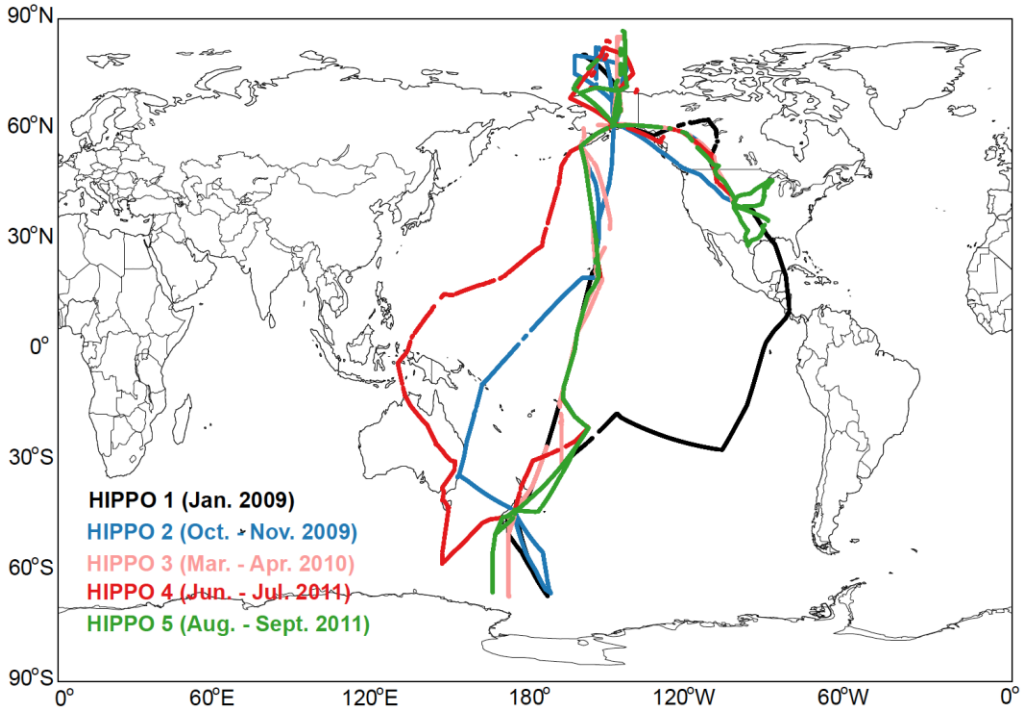

Figure 1. HIPPO aircraft flight tracks in January 2009 (black), October – November 2009 (blue), March – April 2010 (pink), June – July 2011 (red), and August – September 2011 (green).

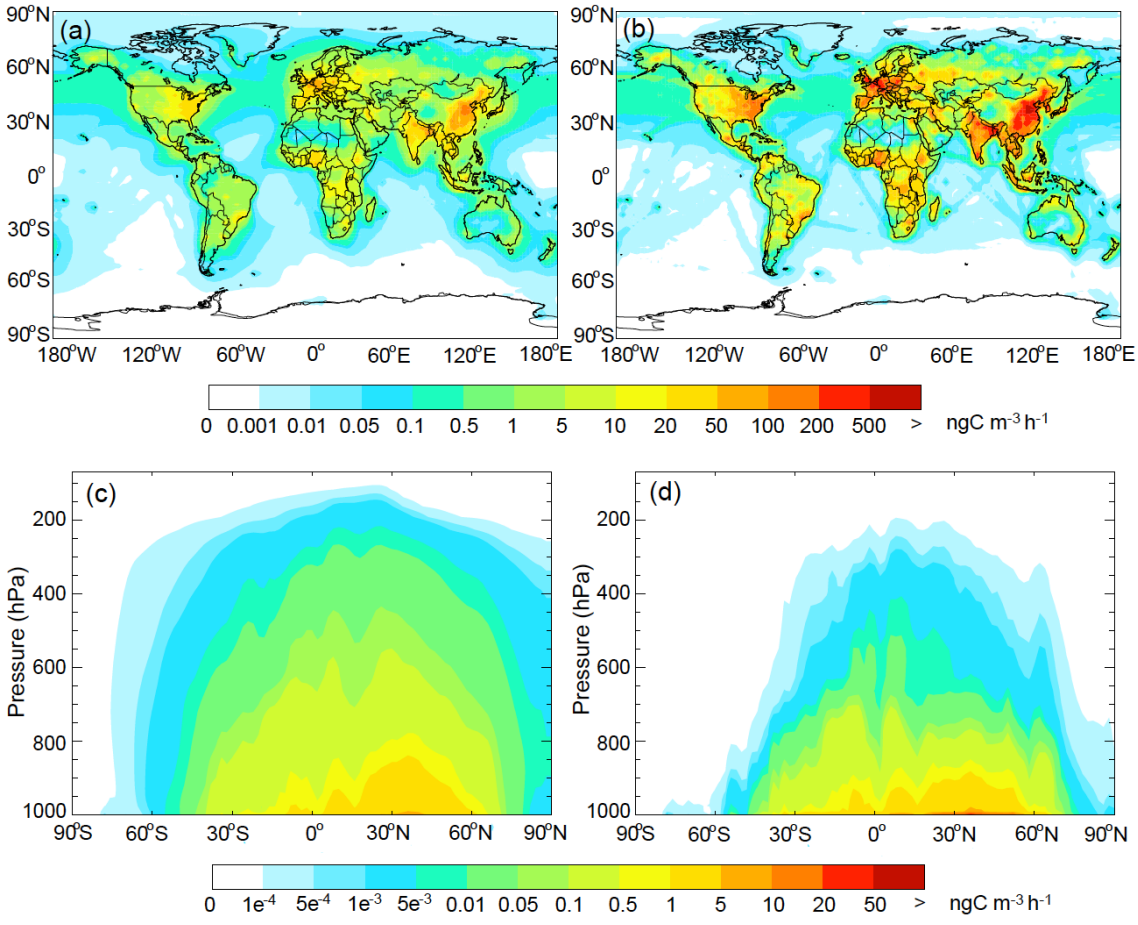

1115

1116

1117 **Figure 2**. GEOS-Chem simulated annual mean BC aging rates (ngC m^{-3} h^{-1}) in the
1118 surface layer (top panels) and averaged zonally (lower panels) from a fixed BC aging
1119 scheme (left panels) and a microphysics-based aging scheme (right panels). See text for
1120 details. Model results are for 2009.

1121

1122

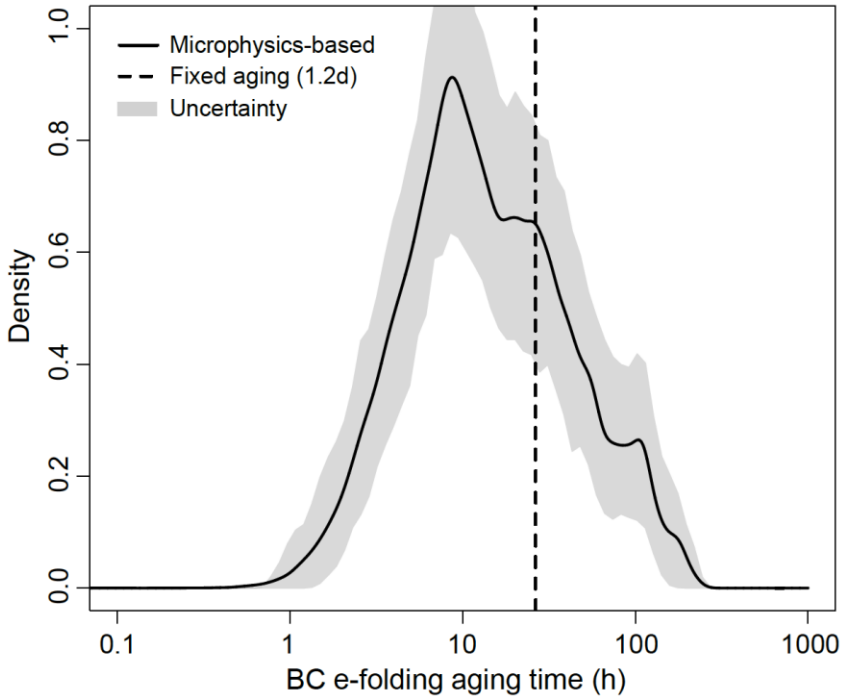

Figure 3. Probability density function of simulated annual mean BC e-folding aging time (h) over the globe for a microphysics-based scheme (solid line) and a fixed aging scheme (dashed line). Also shown is 95% uncertainty range (in grey) of the microphysics-based aging time estimated from a Monte Carlo method.

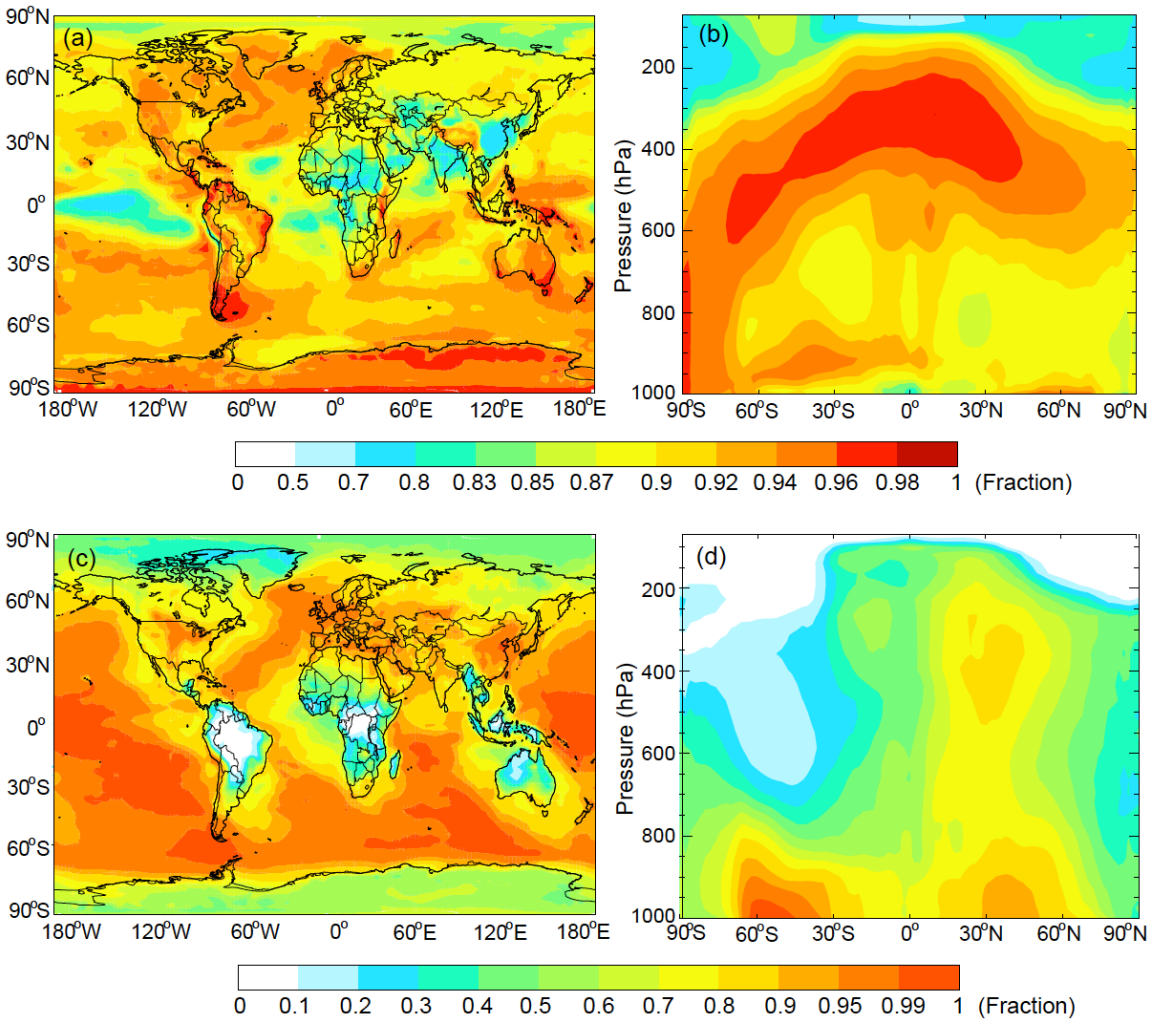

Figure 4. GEOS-Chem simulated annual mean contribution of condensation to total BC aging rate (sum of condensation and coagulation) averaged within 0-1 km above the surface (top left) and zonally (top right) and annual mean contribution of H_2SO_4-HNO_3-NH_3 condensation to the BC aging rate through total condensation (sum of H_2SO_4-HNO_3-NH_3 and SOA condensation) averaged within 0-1 km above the surface (lower left) and zonally (lower right). Model results are for 2009.

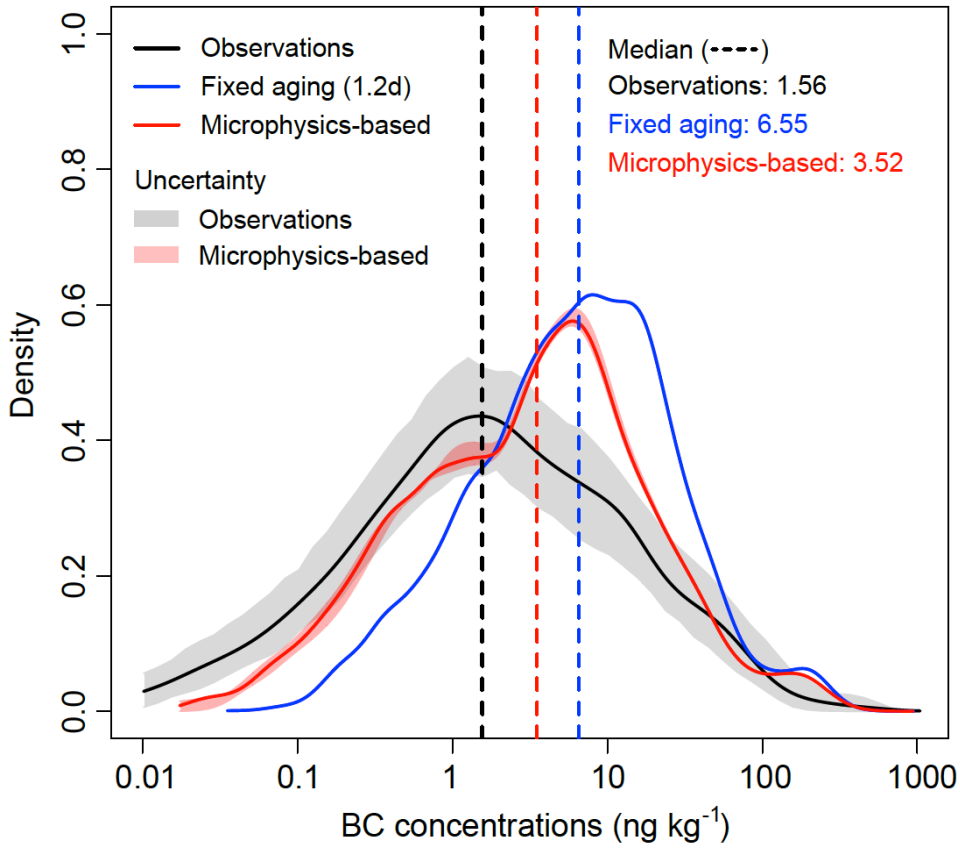

Figure 5. Probability density functions of HIPPO observed (black) and GEOS-Chem simulated BC concentrations. Model results using a fixed BC aging (blue) and a microphysics-based aging (red) are shown. The 95% uncertainty range of the HIPPO observations, estimated from a Monte Carlo method, is shown (in grey). Also shown (in light red) is the range of model results from microphysics-based sensitivity simulations (see Table 1 and text for details). Dashed lines show the median of observations (1.56 ng kg^{-1}, black), fixed aging (6.55 ng kg^{-1}, blue), and microphysics-based aging (3.52 ng kg^{-1}, red). About 5% of the observed BC concentrations are below 0.01 ng kg^{-1}.

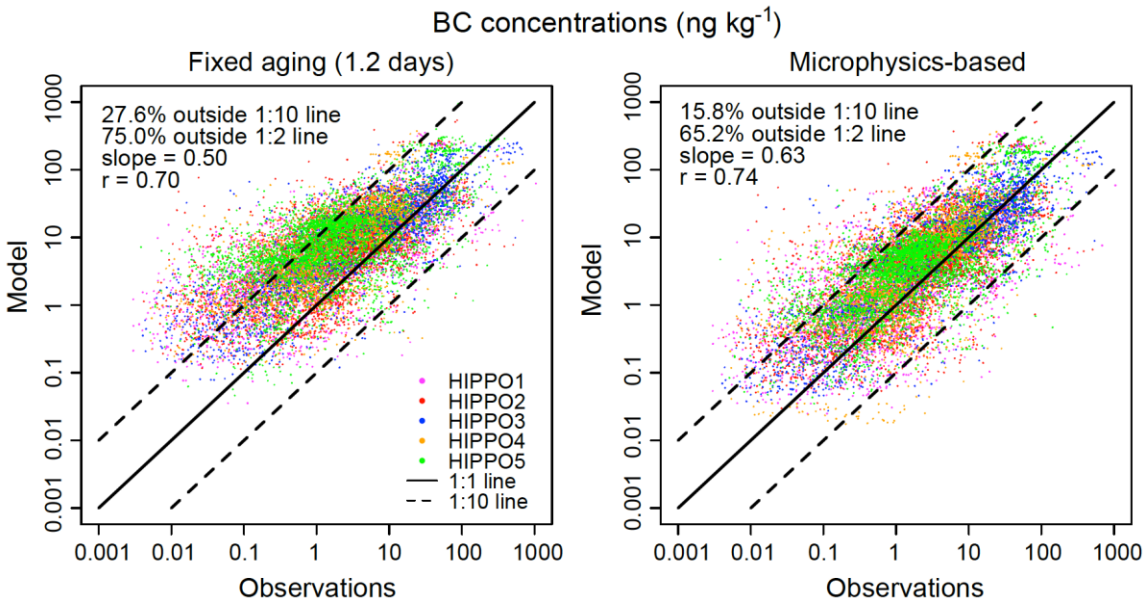

Figure 6. HIPPO observed and GEOS-Chem simulated BC concentrations sampled along the HIPPO flight tracks (HIPPO 1: pink, HIPPO 2: red, HIPPO 3: blue, HIPPO 4: orange, HIPPO 5: green; see Fig. 1), with model results using a fixed BC aging scheme (left panel) and a microphysics-based BC aging scheme (right panel). Also shown are the 1:1 and 1:10 (or 10:1) ratio lines, percentages of data points outside 1:10 (or 10:1) and 1:2 (or 2:1) ratio lines, and slopes and correlation coefficients (*r*) of the regression lines between model results and observations.

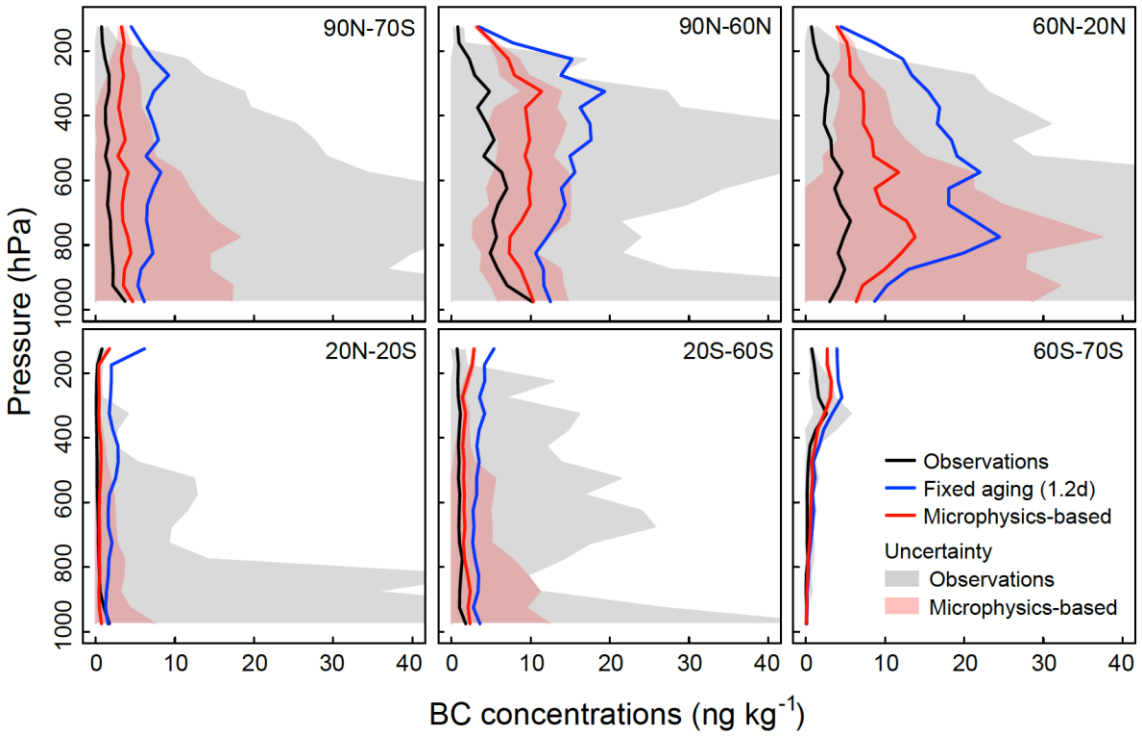

Figure 7. Median vertical profiles of HIPPO observed (black) and GEOS-Chem simulated BC concentrations at different latitudes. Results are averaged over 50 hPa altitude bins. Model results using a fixed BC aging (blue) and a microphysics-based aging (red) are shown. Also shown are the 1-σ uncertainties of observations (grey) and model results (light red) from microphysics-based sensitivity simulations (see Table 1 and text for details).

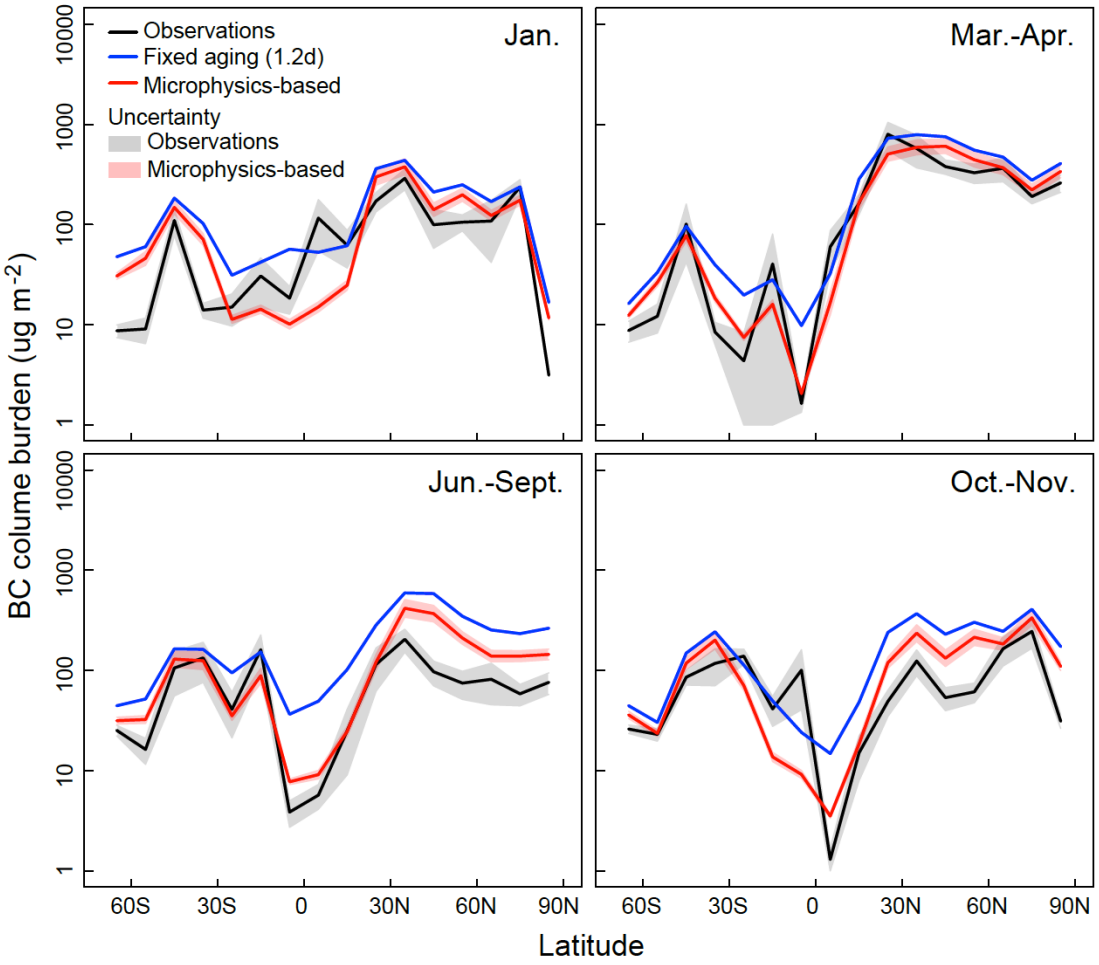

Figure 8. Latitudinal distributions of HIPPO observed (black) and GEOS-Chem simulated BC column burden (μg m^{-2}) in different seasons. The column burden is computed by integrating vertical profiles from the surface to 250 hPa (~10 km) in 10 º latitude bins. Model results using a fixed BC aging (blue) and a microphysics-based aging (red) are shown. Also shown are the 1-σ uncertainties of observations (grey) and model results (light red) from microphysics-based sensitivity simulations (see Table 1 and text for details).

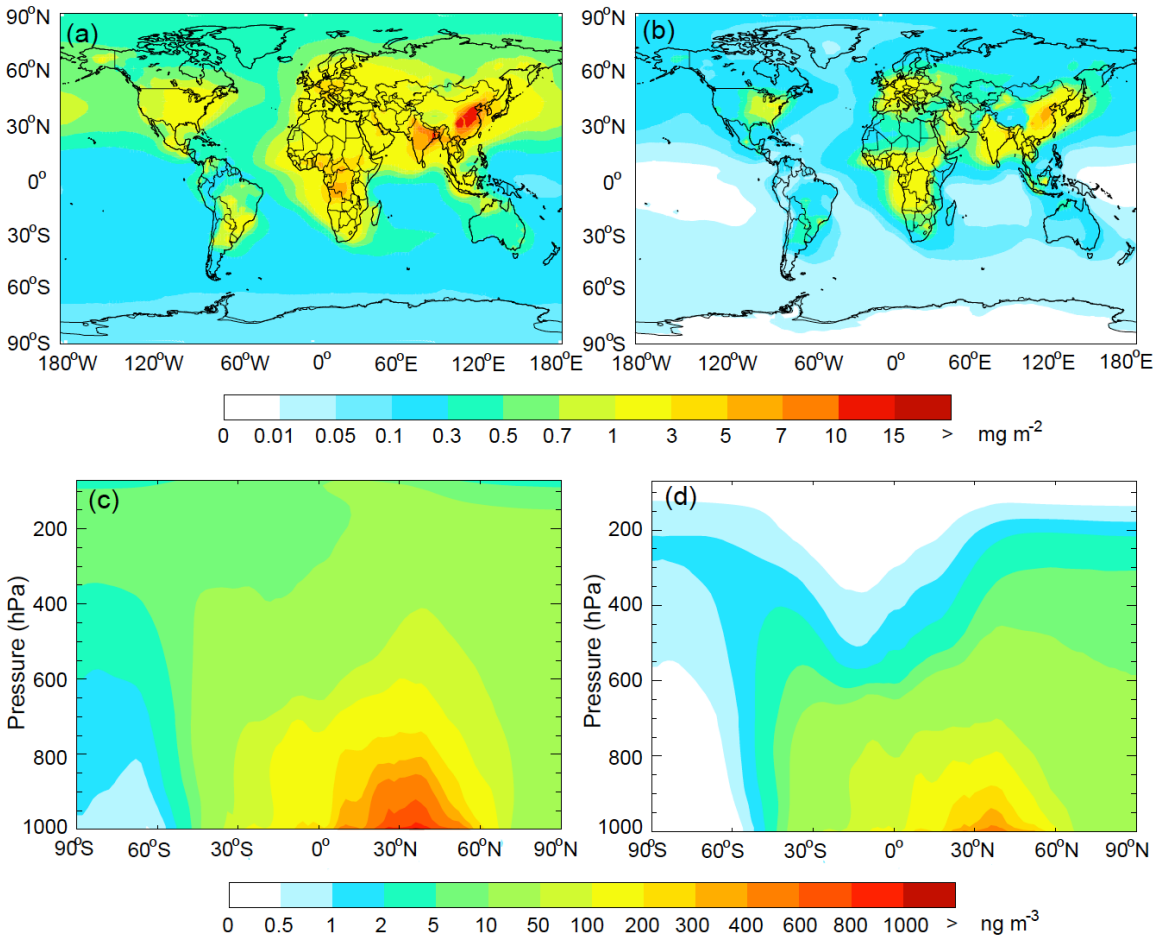

Figure 9. GEOS-Chem simulated annual mean BC column burden (mg m^{-2}) (top panels) and zonal mean BC concentrations (ng m^{-3}) (lower panels) using a fixed BC aging scheme (left panels) and a microphysics-based aging scheme (right panels). Model results are for 2009.

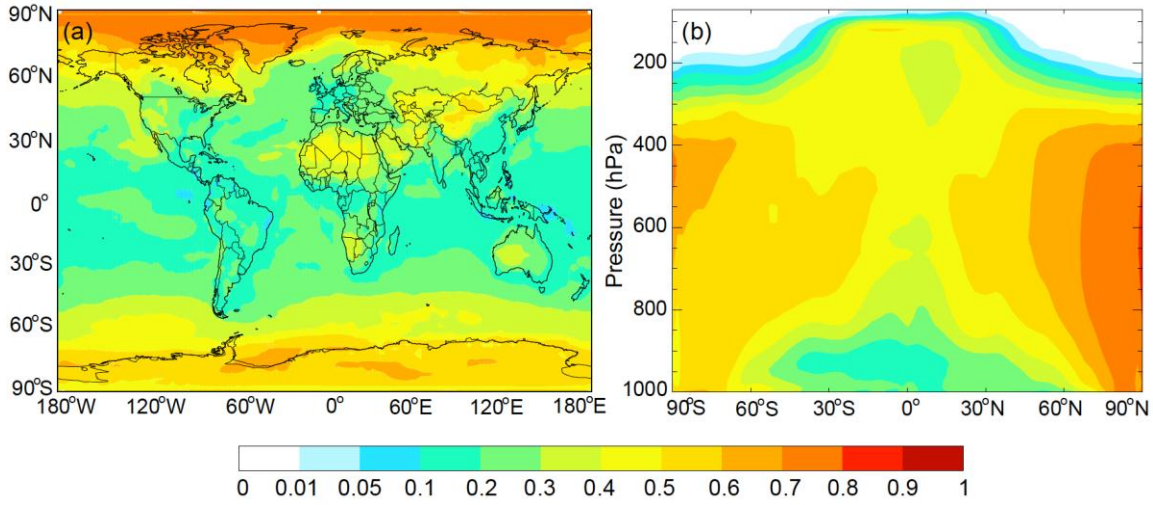

Figure 10. GEOS-Chem simulated annual mean contribution of chemical oxidation to the total BC aging rate (sum of condensation, coagulation, and chemical oxidation) averaged within 0-1 km above the surface (left) and zonally (right). Model results are for 2009.

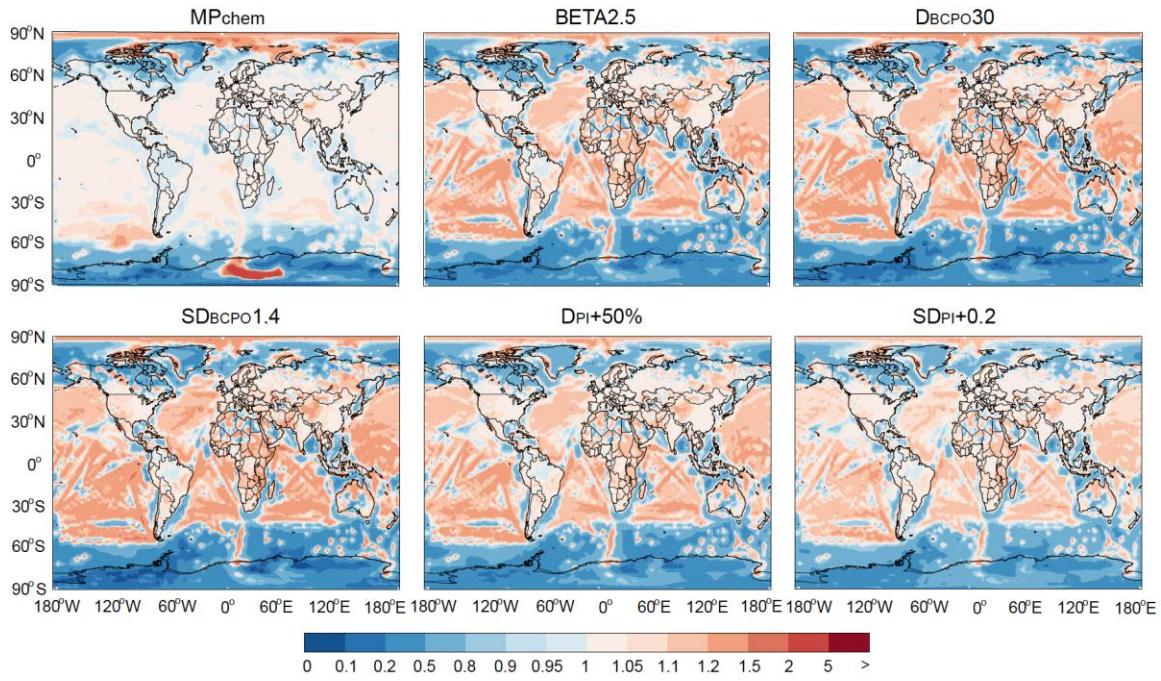

Figure 11. GEOS-Chem simulated ratios of annual mean BC aging rate from six microphysics-based simulations (Table 1) to that from the standard microphysics-based simulation in the surface layer. See Table 1 and text for details. Model results are for 2009.

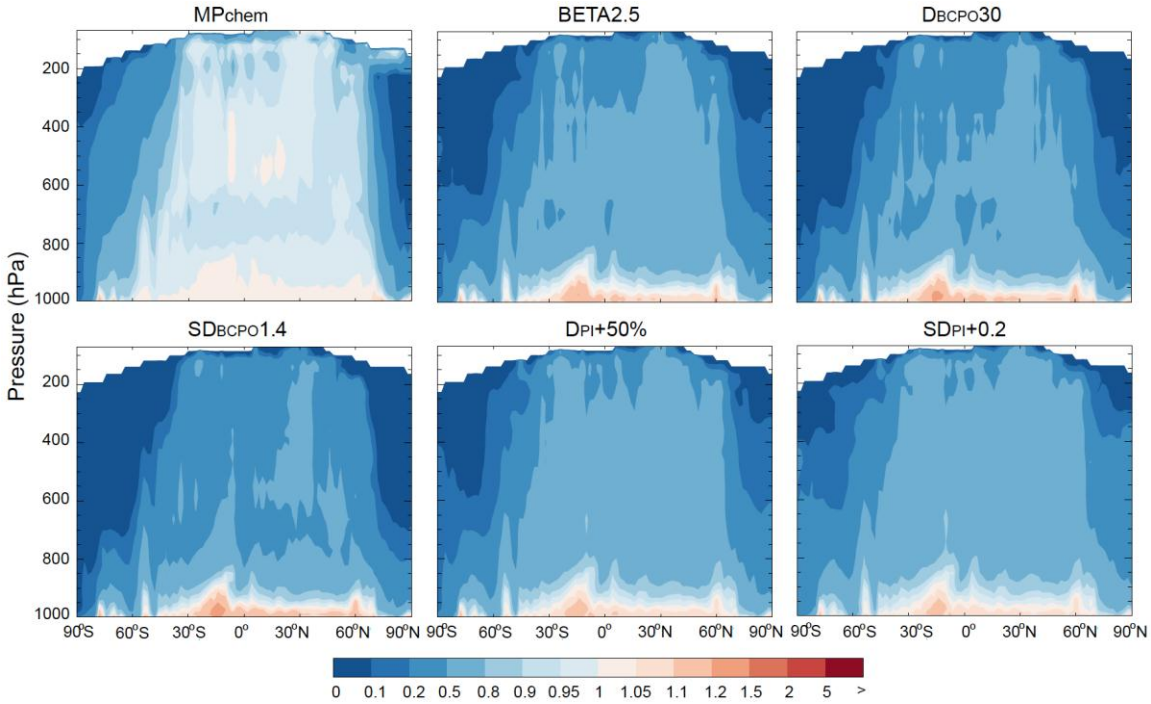

Figure 12. Same as Fig. 11, but for zonal mean BC aging rate.

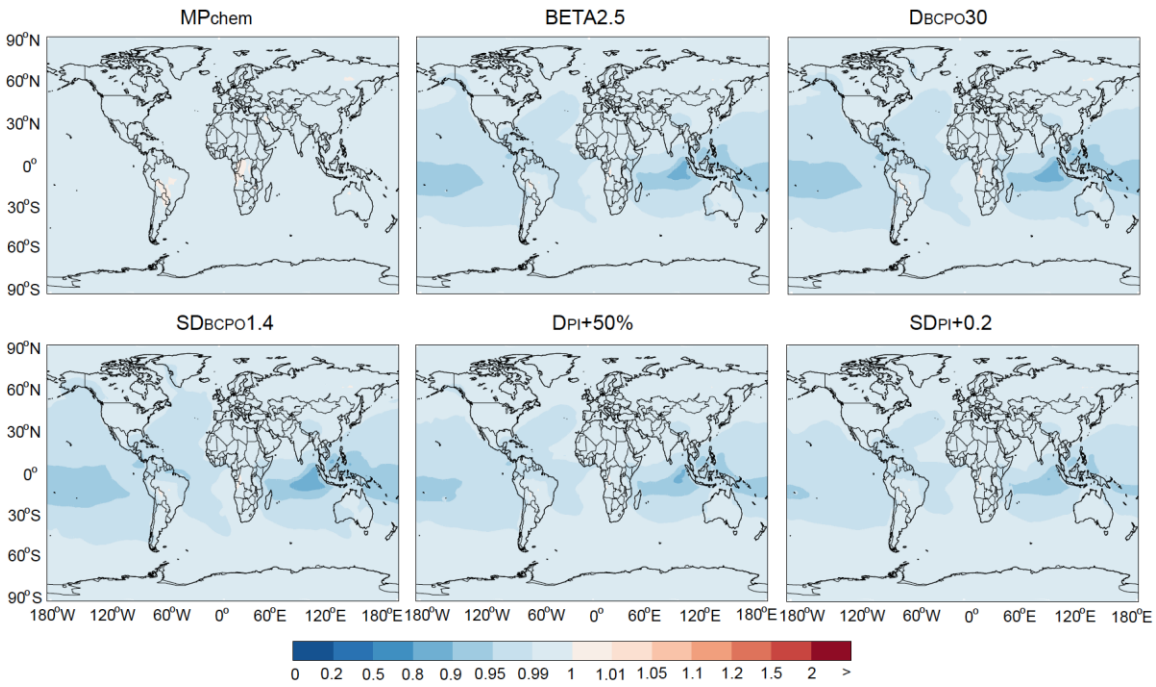

Figure 13. Same as Fig. 11, but for BC column burden.

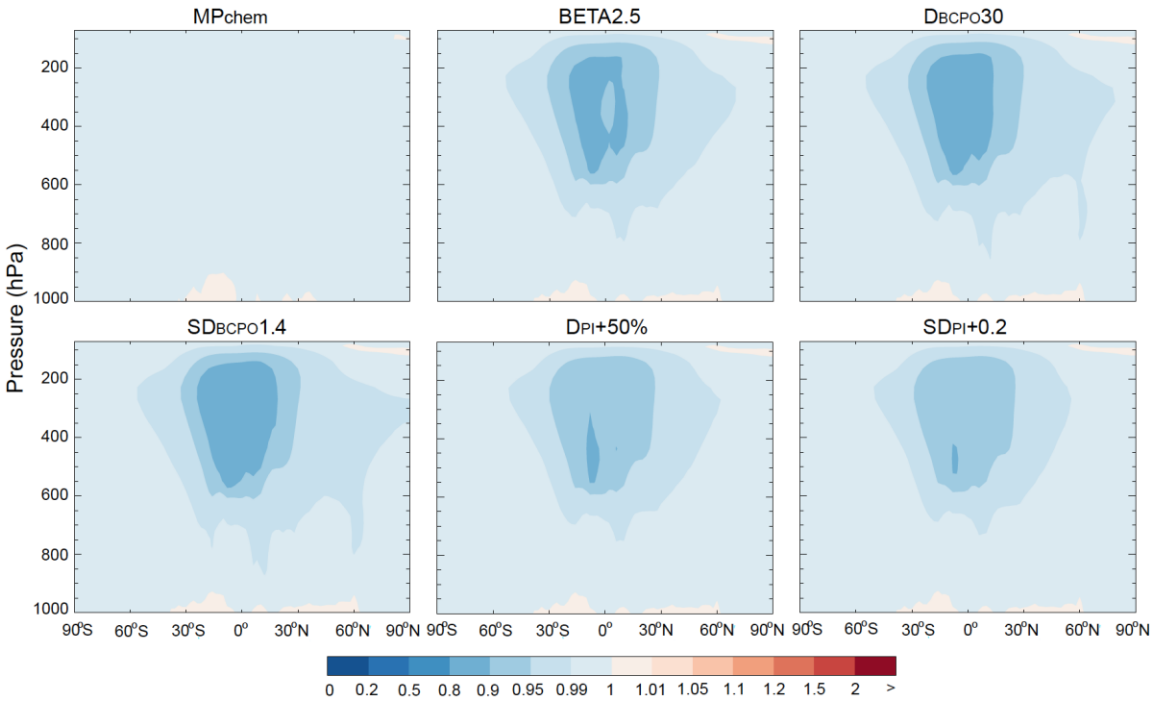

Figure 14. Same as Fig. 12, but for zonal mean BC concentrations.